Interseismic deformation in the Gulf of Aqaba from GPS measurements

Nicolás Castro-Perdomo, Renier Viltres, Frédéric Masson, Yann Klinger, Shaozhuo Liu, Maher Dhahry, Patrice Ulrich, Jean-Daniel Bernard, Rémi Matrau, Abdulaziz Alothman, et al.

Geophysical Journal International

Geophys. J. Int. (2022) **228,** 477–492
Advance Access publication 2021 August 28
GJI Geodynamics and Tectonics

https://doi.org/10.1093/gji/ggab353

Interseismic deformation in the Gulf of Aqaba from GPS measurements

Nicolás Castro-Perdomo [1], Renier Viltres [1], Frédéric Masson [2], Yann Klinger [3], Shaozhuo Liu [1], Maher Dhahry,[4] Patrice Ulrich,[2] Jean-Daniel Bernard,[2] Rémi Matrau,[1] Abdulaziz Alothman,[5] Hani Zahran,[4] Robert Reilinger,[6] P. Martin Mai [1] and Sigurjón Jónsson [1]

[1] *Physical Sciences and Engineering Division, King Abdullah University of Science and Technology (KAUST), Thuwal 23955, Saudi Arabia. E-mail: sigurjon.jonsson@kaust.edu.sa*
[2] *IPGS, EOST Université de Strasbourg, CNRS, Strasbourg,* 67084, *France*
[3] *Institut de Physique du Globe de Paris, Université de Paris, CNRS, F-75005 Paris, France*
[4] *National Center for Earthquakes and Volcanoes, Saudi Geological Survey (SGS), Jeddah,* 21514, *Saudi Arabia*
[5] *King Abdulaziz City for Science and Technology (KACST), Space Research Institute, Riyadh,* 12354, *Saudi Arabia*
[6] *Department of Earth, Atmospheric, and Planetary Sciences. Massachusetts Institute of Technology. Cambridge, MA,* 02139, *USA*

Received 2021 August 14; in original form 2021 March 20

SUMMARY

Although the Dead Sea Transform (DST) fault system has been extensively studied in the past, little has been known about the present-day kinematics of its southernmost portion that is offshore in the Gulf of Aqaba. Here, we present a new GPS velocity field based on three surveys conducted between 2015 and 2019 at 30 campaign sites, complemented by 11 permanent stations operating near the gulf coast. Interseismic models of strain accumulation indicate a slip rate of $4.9^{+0.9}_{-0.6}$ mm yr^{-1} and a locking depth of $6.8^{+3.5}_{-3.1}$ km in the gulf's northern region. Our results further indicate an apparent reduction of the locking depth from the inland portion of the DST towards its southern junction with the Red Sea rift. Our modelling results reveal a small systematic left-lateral residual motion that we postulate is caused by, at least in part, late post-seismic transient motion from the 1995 M_W 7.2 Nuweiba earthquake. Estimates of the moment accumulation rate on the main faults in the gulf, other than the one that ruptured in 1995, suggest that they might be near the end of their current interseismic period, implying elevated seismic hazard in the gulf area.

Key words: Plate motions; Space geodetic surveys; Transient deformation; Continental tectonics: strike-slip and transform; Neotectonics.

1 INTRODUCTION

The highest seismic hazard in Saudi Arabia and Egypt belongs to the areas bordering the Gulf of Aqaba (Fig. 1). This hazard is due to earthquakes on the offshore extension of the Dead Sea Transform (DST), a major fault system that accommodates left-lateral motion between the Arabian plate and the Sinai-Levant subplate (Freund *et al.* 1970; McKenzie 1972). Several major earthquakes are known to have occurred along this southernmost portion of the DST during the last millennium, with the 1995 M_W 7.2 Nuweiba earthquake in the Gulf of Aqaba being the most recent one (Klinger *et al.* 1999; Hofstetter 2003). The decision by the Kingdom of Saudi Arabia to build a megacity in the NEOM area near the gulf has put this region under the spotlight, requiring further research efforts to improve the seismic hazard knowledge of the gulf area.

The DST formed as a result of the mid-Cenozoic breakup of the Arabo-African plate, and today it extends roughly 1000 km from the Red Sea rift to the East Anatolian fault (Garfunkel 1981). The total estimated left-lateral offset of the DST south of the Dead Sea is about 105 km (e.g. Quennell 1958, 1959; Freund *et al.* 1970; McKenzie *et al.* 1970; Garfunkel 1981; Joffe & Garfunkel 1987) and the onset of its left-lateral strike-slip motion post-dates 19–22 Ma (e.g. Bar *et al.* 1974; Steinitz *et al.* 1978; Bartov *et al.* 1980; Eyal *et al.* 1981; Joffe & Garfunkel 1987; Ben-Avraham *et al.* 2012; Nuriel *et al.* 2017). These estimates translate to an average slip rate between 4.8 and 5.5 mm yr^{-1} since the initiation of fault motion along the southern part of the DST comprising the Jordan Valley and Wadi Arabah faults.

The geomorphology along the strike of the DST is marked by a series of pronounced depressions, 5–20 km wide,

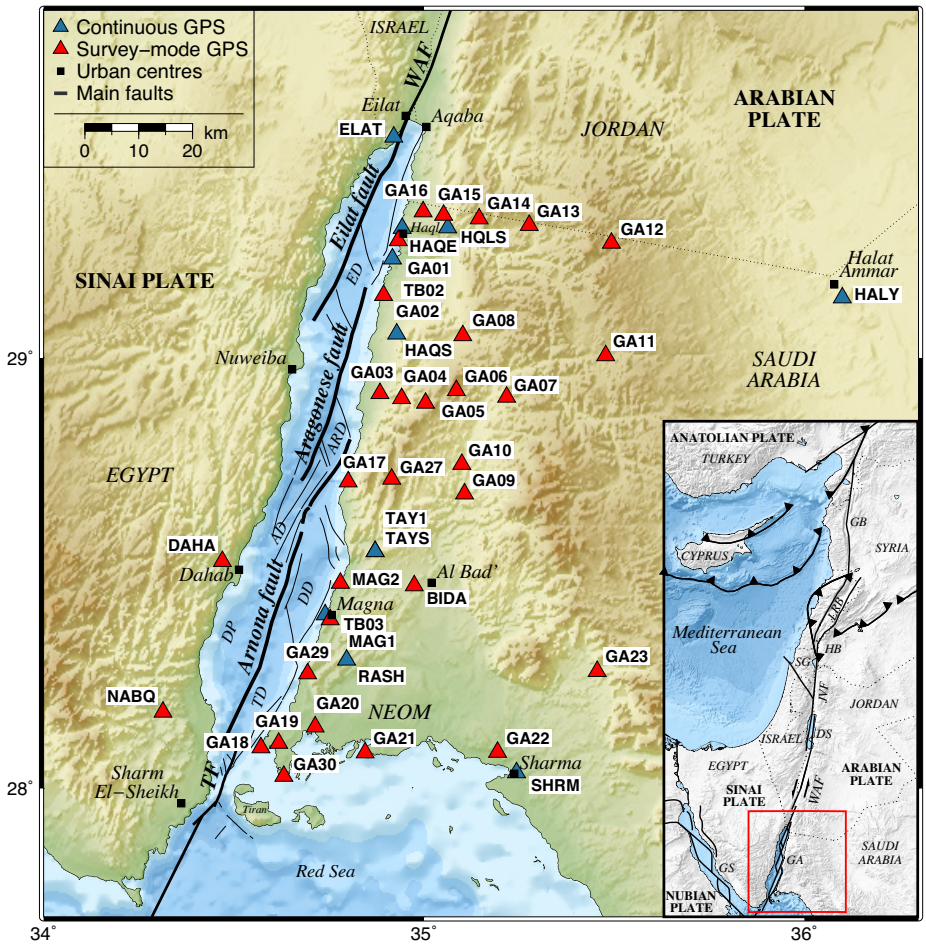

Figure 1. Mapped faults in the Gulf of Aqaba along with the GPS stations used in this study. Permanent and campaign GPS sites are shown as blue and red triangles, respectively. Fault traces and pull-apart basins are based on Ribot *et al.* (2021). The inset shows the area of interaction of the Arabian, Nubian, Sinai and Anatolian plates. Shaded topography is based on the SRTM30 PLUS digital elevation model (Becker *et al.* 2009) and regional-scale fault traces in the inset are compiled from Le Béon *et al.* (2008). TD, Tiran Deep; TF, Tiran Fault; DP, Dahab Plateau; DD, Dakar Deep; AD, Arnona Deep; ARD, Aragonese Deep; ED, Eilat Deep; GS, Gulf of Suez; GA, Gulf of Aqaba; WAF, Wadi Arabah Fault; DS, Dead Sea; JVF, Jordan Valley Fault; SG, Sea of Galilee; HB, Hula Basin; LRB, Lebanese Restraining Bend; GB, Ghab Basin.

corresponding to pull-apart basins. These morphological depressions form at jogs between discontinuous segments of the DST and are usually delimited by both normal and strike-slip faults (e.g. Garfunkel 1981; Ben-Avraham & Zoback 1992; Klinger *et al.* 1999; Ben-Avraham *et al.* 2012). From north to south, these depressions comprise the Ghab and Hula basins, the Sea of Galilee, the Dead Sea and the Gulf of Aqaba (see inset in Fig. 1. This series of pull-apart basins formed by left-lateral shear along left-stepping en échelon fault segments, which results in rhomb-shaped grabens subjected to left-lateral shear and extension, Quennell 1959; Garfunkel 1981). Despite being primarily a transtensional fault system (Garfunkel 1981), a major ∼200 km long restraining bend characterizes the central part of the DST in Lebanon and Syria (e.g. Heimann & Ron 1987; Gomez *et al.* 2007). This segment deviates 20°–30° from the main trend of the DST and accounts for ∼1.6 mm yr^{-1} of convergent motion between the Sinai and Arabian plates at that latitude (e.g. Elias *et al.* 2007; Gomez *et al.* 2007).

Historical records, palaeoseismic trenching and geomorphological studies indicate that many destructive earthquakes have occurred along the DST over the past two millennia (e.g. Ambraseys 2009; Agnon 2014; Meghraoui 2015; Klinger *et al.* 2015; Lefevre *et al.* 2018). Two successive earthquakes occurred in 363 AD, affecting more than 20 towns in Palaestine and Syria (Ambraseys 2009). According to Thomas *et al.* (2007), these earthquakes caused extensive destruction at several localities in southern Wadi Arabah. This observation is in agreement with Klinger *et al.* (2015), who reported an event horizon in a trench located 30 km north of the city of Aqaba (Jordan) that could be related to these earthquakes.

A major historical earthquake occurred in 1068 AD in the gulf area, destroying the town of Eilat (Ambraseys 2009). Zilberman *et al.* (2005) reported that the earthquake was strong enough to rupture the surface along the Eilat fault, affecting an irrigation system. Historical records document another violent earthquake in 1212 AD. This earthquake was strongly felt in Eilat and caused damages to the monastery of St Catherine in the Sinai Peninsula (Ambraseys 2009). This event was identified in a trench close to the village of Qatar in southern Jordan (Klinger *et al.* 2015), and a brecciated layer associated with this earthquake was also reported by Kagan *et al.* (2011) in the Dead Sea basin. The last major historical earthquake reported in the gulf area occurred in 1588. Despite its location and magnitude are a subject of debate, intense shaking was documented as far as Cairo and Madinah, suggesting an epicentre in the northern Red Sea region (Ambraseys 2009). Finally, the largest instrumental

earthquake along the entire DST was the M_W 7.2 Nuweiba Earthquake, which struck the Gulf of Aqaba area on 1995 November 22, causing significant damage in nearby coastal communities in Egypt, Saudi Arabia, Jordan and Israel (Klinger *et al.* 1999; Hofstetter 2003).

The gulf itself is about 180 km long and up to 25 km wide (Ben-Avraham *et al.* 1979; Garfunkel 1981), and its structure is dominated by three left-stepping en échelon faults bounding a series of pull-apart basins (Ben-Avraham *et al.* 1979; Ben-Avraham 1985; Ribot *et al.* 2021, Fig. 1). The northernmost fault segment within the gulf is the Eilat fault. This fault is approximately 59 km long and constitutes the western boundary of the Eilat deep. The central fault segment is the Aragonese fault, which extends approximately 53 km, bounding the Eilat deep to the east and the Aragonese deep to the west. The Arnona fault constitutes the southernmost segment, extending roughly 83 km and forming the western boundary of the Dakar and Tiran deeps. Compelling evidence indicates that the Aragonese fault segment ruptured during the Nuweiba earthquake, while the other segments have not released significant seismic moment in the past several centuries (Shamir *et al.* 2003; Hofstetter 2003; Baer *et al.* 2008; Ribot *et al.* 2021).

The seismic activity in the gulf is characterized by the occurrence of swarms, which have been observed since the deployment of the first regional seismic networks in the area (El-Isa *et al.* 1984; Alamri *et al.* 1991) as cited in Klinger *et al.* (1999). Significant swarm activity was reported in 1983, 1990 and 1993, reaching M_W 6.1 (El-Isa *et al.* 1984; Pinar & Tükelli 1997; Klinger *et al.* 1999, Fig. 2). Most earthquakes in the gulf exhibit predominantly left-lateral motion. However, some of them show significant normal motion, as evidenced by the pure normal slip reported for the largest event during the 1993 earthquake swarm (Klinger *et al.* 1999; Hofstetter 2003). More recently, in 2015 June, an M_W 5.2 strike-slip earthquake struck the gulf area, causing strong shaking in nearby communities and an aftershock sequence that lasted for more than two weeks (El-Aal & Badreldin 2016). Recent seismic data collected by the Saudi Geological Survey (SGS) show that earthquakes concentrate along, and are subparallel to the gulf fault system, as shown in Fig. 2.

The present-day crustal deformation along the DST north of the Gulf of Aqaba has been extensively analysed in terms of interseismic strain accumulation (e.g. McClusky *et al.* 2003; Wdowinski *et al.* 2004; Gomez *et al.* 2007; Le Béon *et al.* 2008, 2010; Al Tarazi *et al.* 2011; Le Béon *et al.* 2012; Sadeh *et al.* 2012; Mahmoud *et al.* 2013; Masson *et al.* 2015; Hamiel *et al.* 2016, 2018a). However, only four GPS studies have provided slip rate estimates across the fault system in the gulf area. By implementing a back-slip model, Mahmoud *et al.* (2005) derived a slip rate of 4.4 $\pm$ 0.3 mm yr^{-1}, assuming a fixed locking depth of 13 km. A similar approach was followed by Reilinger *et al.* (2006), who reported a slip rate of 4.5 $\pm$ 0.3 mm yr^{-1}, holding the locking depth fixed to 12 km. ArRajehi *et al.* (2010) estimated slip rates of 4.8 $\pm$ 0.2 mm yr^{-1} in the gulf, and, more recently, Gomez *et al.* (2020) implemented a back-slip model and reported a slip rate of 4.9 $\pm$ 0.1 mm yr^{-1}. Unfortunately, these studies were unable to provide locking depth estimates due to the limited geodetic coverage near the gulf.

In this study, we use previously unpublished geodetic data to derive an updated crustal motion velocity field of the gulf. We further implement standard models of interseismic deformation to investigate the fault kinematics along the offshore segments of the DST fault system. Finally, we consider four possible model scenarios of time-dependent viscoelastic deformation produced by the Nuweiba earthquake and discuss whether post-seismic transient motions are evidenced in the GPS data acquired near the gulf.

2 GPS DATA AND ANALYSIS

A new survey-mode GPS network was installed in 2014 and surveyed three times in 2015 February, 2017 March and 2019 May (see Table S1 and Fig. S1, Supporting Information). This network consists of 27 GPS markers distributed over an area of 150 km by 70 km on the eastern gulf coast, extending from the Strait of Tiran in the south to the Jordan border in the north (Fig. 1). During the surveys, we also occupied three older markers installed by MIT near the municipalities of Al Bad' and Magna (sites BIDA, MAG1 and MAG2). These stations were measured annually between 2010 and 2014 (Gomez *et al.* 2020), and their data were reprocessed in our study. We also analysed the GPS data collected between 2000 and 2005 at the campaign sites DAHA and NABQ, which are located near the gulf coast on the Sinai Peninsula (McClusky *et al.* 2003; Mahmoud *et al.* 2005; Gomez *et al.* 2020).

To better understand the relative motion between the Sinai-Levant subplate and the Arabian plate, we processed data from 20 stations of the GIL network of continuous GPS monitoring in Israel (Wdowinski *et al.* 2001), covering a 19-yr analysis period from 2000 to 2019 (see Fig. S2, Supporting Information). Considering the rapid expansion of continuous GPS networks in Saudi Arabia, we incorporated data from additional 11 permanent stations near the gulf (HAQS, HQLS, TAY1, HAQE, SHRM, BEJD, TB02, TB03, HALY, RASH and TAYS). Our research significantly improves the GPS station coverage near the Gulf of Aqaba compared to previous studies, which relied on sparse GPS data in this area (e.g. McClusky *et al.* 2003; Mahmoud *et al.* 2005; Reilinger *et al.* 2006; ArRajehi *et al.* 2010; Gomez *et al.* 2020). Nevertheless, near-fault GPS observations are limited to distances greater than 8 km due to the presence of the gulf itself and the lack of offshore geodetic measurements.

We analysed the GPS data using the GAMIT/GLOBK software package version 10.70 (Herring *et al.* 2018) following a three-step approach described in detail by Dong *et al.* (1998). Daily carrier phase data from campaign and permanent stations were analysed separately to improve the processing efficiency (e.g. Bock *et al.* 1997). Following this strategy, we obtained two sets of loosely constrained solution vectors and covariance matrices. Both solutions share a set of 16 reference sites with well-determined coordinates and velocities, which we used to tie our final combined solution to the International Terrestrial Reference Frame (ITRF) 2014 (Altamimi *et al.* 2017). Campaign solutions were then merged with the continuous ones to get a final solution with ambiguities resolved and loose constraints on estimated parameters.

Combined solutions were used to estimate position time series and site velocities in GLOBK. The reference frame realization was achieved by imposing tight constraints to the coordinates and velocities of 16 sites that comprise the reference network (ZIMM, GRAZ, ONSA, JOZE, WSRT, KIT3, IISC, POLV, ARTU, POL2, MAS1, RABT, YEBE, DGAR, MBAR and NKLG), minimizing in an iterative scheme their position adjustments with respect to their ITRF2014 *a priori* coordinates by estimating a six-parameter Helmert transformation. Finally, we accounted for time-correlated errors in the position time-series by characterizing their noise spectrum using the Hector software package version 1.7.2 (Bos *et al.* 2013). Since campaign stations do not have enough observations to estimate the time-correlated noise in their position time-series, we used the mean random walk values obtained for the permanent stations in the study area (4.5 10^{-7} and 1.5 10^{-6} m^2 yr^{-1} for the horizontal and vertical velocity components, respectively). Following this approach, the resulting horizontal velocity uncertainties for stations within the new campaign GPS network deployed near the

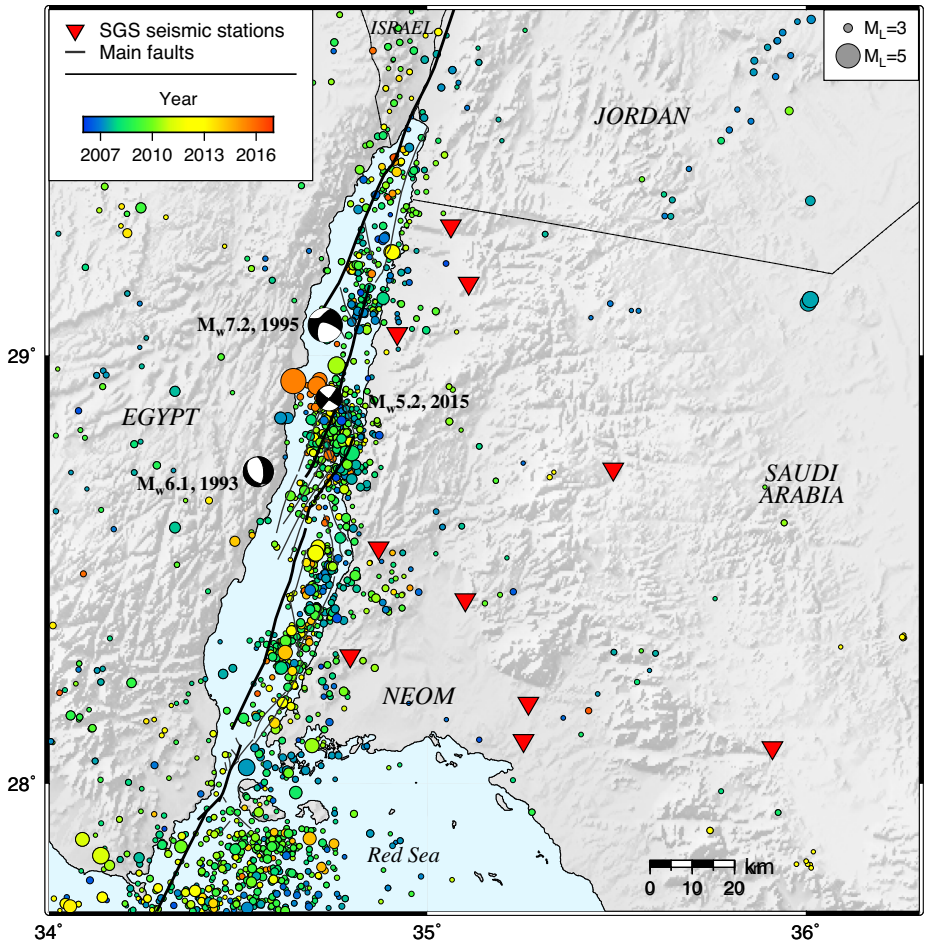

Figure 2. Earthquake locations ($M_L \geq 1.5$) in the Gulf of Aqaba region from 2006 January to 2016 March with circle sizes scaled according to earthquake magnitude and colours according to date. Focal mechanisms of the 1993 M_W 6.1, 1995 M_W 7.2 and 2015 M_W 5.2 earthquakes are from the National Earthquake Information Center (NEIC, https://earthquake.usgs.gov), the Global Centroid-Moment-Tensor (GCMT) catalogue (Dziewonski *et al.* 1981; Ekström *et al.* 2012) and El-Aal & Badreldin (2016), respectively. Seismic stations operated by the SGS are shown as red inverted triangles. Note that the one-sided geometry of the SGS seismic network might bias epicentral locations.

gulf vary between 0.5 and 1.0 mm yr^{-1} (see Table S2, Supporting Information).

3 GPS VELOCITY FIELD

Time-series and site velocities realized in ITRF2014 were rotated into stable Sinai reference frame. To perform this rotation, we estimated the Euler pole of the Sinai subplate with respect to ITRF2014 using five reliable stations located on the Sinai subplate at distances greater than 40 km from the DST (CSAR, ALON, YRCM, BSHM and RAMO), as shown in Fig. S2 in the Supporting Information. The SINAI-ITRF2014 Euler pole derived here is 54.7±0.7° N, 347.8±4.0° E, $\omega = 0.417 \pm 0.021°$ Ma^{-1}, which is consistent with Euler vectors estimated in earlier studies (e.g. Wdowinski *et al.* 2004; Le Béon *et al.* 2008; Sadeh *et al.* 2012; Hamiel *et al.* 2016, 2018a, 2018b; Hamiel & Piatibratova 2019). Observed GPS horizontal velocities for the sites on the Arabian plate show NNE motion relative to Sinai (Fig. 3), as reported in previous geodetic investigations (e.g. ArRajehi *et al.* 2010; Sadeh *et al.* 2012; Gomez *et al.* 2020). The velocity field thus reflects the left-lateral motion of the DST fault system. The increasing DST-parallel velocities towards the interior of the Arabian plate in this Sinai-fixed reference frame (Figs 3–5a) suggest that the coastal areas bordering the gulf faults are currently undergoing interseismic strain accumulation.

Fig. 4 shows profiles of fault-parallel and fault-normal components of GPS-derived velocities relative to the Sinai-Levant subplate. These projections were performed assuming a single vertical fault with a strike of N16° E extending from the Strait of Tiran in the south to the northernmost tip of the gulf (dashed yellow line in Fig. 3). Increasing DST-parallel velocities towards the Arabian plate support active interseismic strain accumulation along the coastal areas adjacent to the gulf (Fig. 4a). We further note that the mean fault-normal velocity considering all the stations on the Arabian side of the gulf is $\sim$ 0.8 mm yr^{-1} (Fig. 4b). This observation is consistent with a partly divergent motion between the Sinai and Arabian plates at this latitude, as suggested in previous investigations (e.g. Mahmoud *et al.* 2005; Reilinger *et al.* 2006; Gomez *et al.* 2020). However, the scatter observed in both velocity profiles suggests that the assumption of a single fault along the full extension of the gulf may be inadequate. This observation led us to consider different fault traces within the gulf based on the structural maps by Ben-Avraham (1985) and Ribot *et al.* (2021), see below.

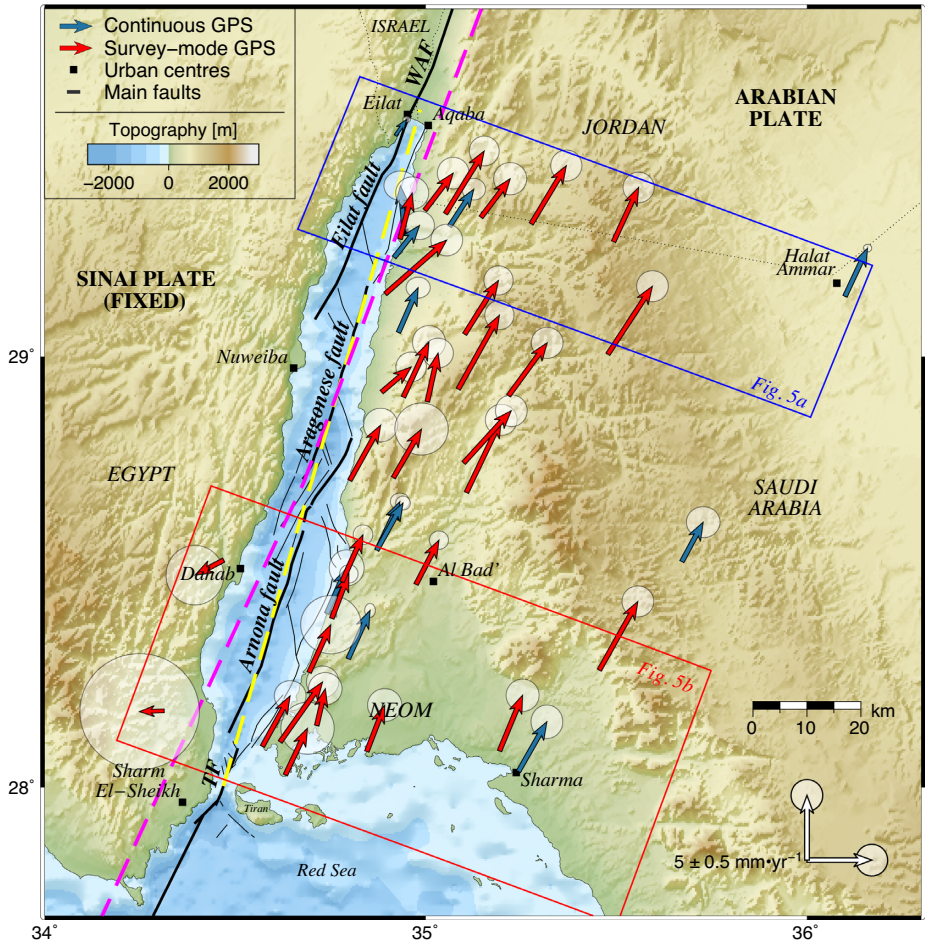

Figure 3. Horizontal GPS velocities relative to Sinai with 95 per cent confidence ellipses. Permanent and campaign site velocity vectors are coloured in blue and red, respectively. The blue and red boxes indicate the location of the velocity profiles shown in Figs 5(a) and (b). The dashed yellow line corresponds to the assumed fault location used in Figs 4(a) and (b). The dashed magenta arc delineates the small circle around the Arabia-Sinai Euler pole derived in this study.

4 ELASTIC DISLOCATION MODEL

We conducted an initial kinematic assessment of the GPS velocity field across the gulf by implementing a screw dislocation model (e.g. Weertman & Weertman 1964; Savage & Burford 1973). Following this approach, theoretical fault-parallel velocities v can be expressed as follows:

$$v = a + \frac{b}{\pi} \tan^{-1}\left(\frac{x}{D_L}\right) \quad (1)$$

where a defines the vertical origin of the arctangent curve, and x is the perpendicular distance measured from the fault trace. The fault is assumed to be locked during the interseismic period at depths extending from the surface down to a depth D_L (often referred to as locking depth), below which free slip occurs at a rate equivalent to the secular relative plate motion b. GPS measurements at distances within one-half the locking depth are required to accurately constrain fault locking depths, whereas far-fault observations are important to constrain secular slip rates (Smith-Konter *et al.* 2011). This simple interseismic model has been extensively used to investigate kinematic parameters of many strike-slip and transform faults globally (e.g. Lisowski *et al.* 1991; Wright *et al.* 2001; Reilinger *et al.* 2006; Sadeh *et al.* 2012).

Here we analyse two velocity profiles across the Eilat fault in the north, and the Arnona and Tiran faults (TF) in the south, which include the largest number of near-fault GPS stations. The northern profile extends from the city of Eilat at the northern tip of the gulf to the municipality of Halat Ammar, located 120 km inside the Arabian plate (Fig. 5a), assuming a fault strike of N22° E. The southern profile extends from Sharm El-Sheikh in the Sinai Peninsula to the city of Sharma in Saudi Arabia (Fig. 5b), and assumes a fault strike of N20° E. The sampling width of these profiles is based on the extension of the fault segments within the gulf, which overlap in certain areas forming pull-apart basins, as shown in Fig. 1. Following this criterion, the southern Eilat and the Aragonese pull-apart basins correspond to the limits of the northern and southern profiles, respectively. Unlike the northern and southern profiles, the central area across the Aragonese fault does not include enough near- and far-field GPS stations to reliably constrain slip rates and locking depths. Moreover, there are no stations constraining GPS rates on the Sinai Peninsula west of the Aragonese fault. For these reasons, the central segment was not considered for slip-rate and locking depth inversions.

We constrained model parameters (i.e. a, b and D_L) and their uncertainties using a grid-search algorithm coupled with a Monte Carlo procedure that accounts for uncertainties in the fault position

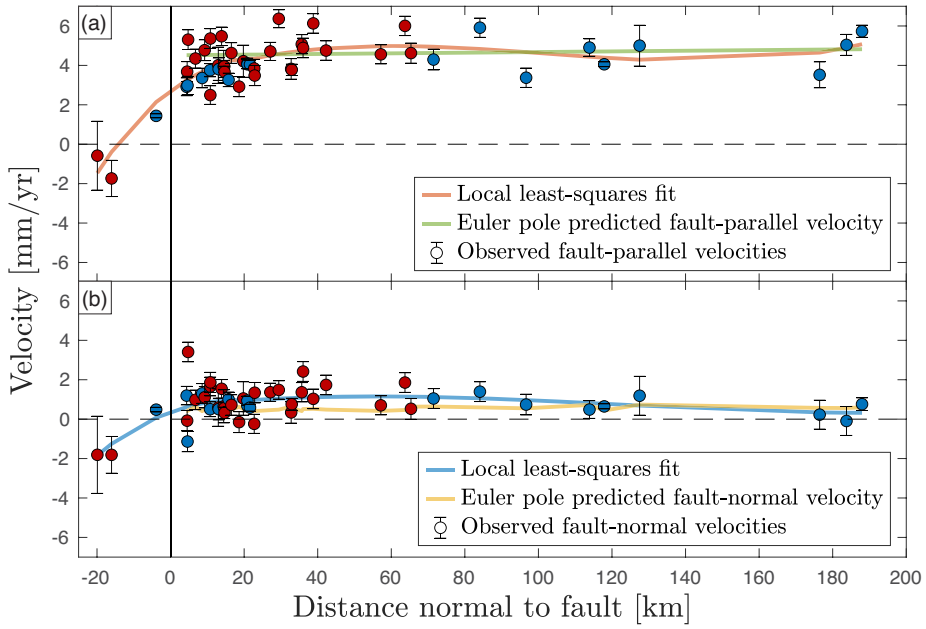

Figure 4. Profiles of (a) fault-parallel and (b) fault-normal velocities across Gulf of Aqaba assuming a single vertical fault striking N16° E along the gulf (dashed yellow line in Fig. 3). Site velocities are expressed in a Sinai-fixed reference frame, that is, positive velocity values on the Arabian plate ($x > 0$) represent left-lateral motion in (a) and opening in (b) across the gulf. The solid orange and blue lines correspond to the best local least-squares fit to fault-parallel and fault-normal velocities, respectively. The least-squares fit was performed using a third-order Savitzky–Golay filter considering 39 data points per window. The pale green and yellow lines represent the fault-parallel and fault-normal velocities predicted by the Arabia-Sinai Euler Pole. Permanent and campaign site velocities are coloured in blue and red, respectively.

and stations' velocities. The best fit corresponds to the set of model parameters that results in the lowest root mean squared (RMS) error relative to the actual GPS observations (Figs 5a and b). To estimate uncertainties in slip rates and locking depths, we conducted 10^4 Monte Carlo simulations, perturbing the location of the fault randomly within a range of ±0.5 km and adding Gaussian noise to the GPS velocities within their 1-sigma uncertainties. In each Monte Carlo simulation, the grid-search explores the misfit (RMS) of the model for a range of values in the parameter domain, and selects the combination of model parameters that results in the lowest misfit. The strike (azimuth) of the fault segments was held fixed during the slip rate and locking depth inversions. However, we explored the effect of small perturbations (±5°) in fault strike on the final inversion results. We found that small variations in fault strike do not have a statistically significant impact on the slip rate and locking depth estimates, as shown in Fig. S3 in the Supporting Information.

After performing the Monte Carlo inversion, we derived a 2×2 covariance matrix from the resulting distribution of slip rates and locking depths. From this covariance matrix, we estimated the width (ω) and height (h) of the confidence level ellipse, which are given by $\omega = 2 \times nstd \times \sqrt{\lambda_1}$ and $h = 2 \times nstd \times \sqrt{\lambda_2}$, where $nstd$ represents the desired confidence level (in standard deviations) and $\lambda_{1,2}$ are the eigenvalues of the covariance matrix. We followed this approach to derive 1-sigma (68 per cent) confidence level ellipses, as shown in Figs 5(c) and (d).

Our results yielded a slip rate of $4.9^{+0.9}_{-0.6}$ mm yr^{-1} and a locking depth of $6.8^{+3.5}_{-3.1}$ km for the northern profile across the Eilat fault (red curve Fig. 5a). Further south, across the Arnona fault and TF, we derived a slip rate of $5.5^{+1.3}_{-0.9}$ mm yr^{-1} and a locking depth of $0.8^{+3.4}_{-0.8}$ km (red curve in Fig. 5b). Stations GA12, GA13 and GA15 in the northern profile and GA19, GA20 and GA23 in the southern profile exhibit anomalous rates relative to nearby stations with no obvious explanation. These outliers could be related to local effects that may include unmodelled tropospheric signals, local deformation and seasonal loading, which are not modelled for the campaign stations. The inclusion of sites with anomalous behaviour in the slip rate and locking depth inversion is undesirable because they adversely affect fit to the data (e.g. Sadeh *et al.* 2012). For this reason, these stations were dismissed from the analysis, yielding the results given by the red curves in Figs 5(a) and (b).

To further analyse the effect of near-fault station rates on the final locking depth estimates, we considered additional scenarios omitting stations GA01 and GA16 in the northern profile and GA18 in the southern profile (blue curves in Figs 5a and b). Our results show that the omission of sites GA01 and GA16 in the northern profile has a minor effect on the slip rate estimate but results in a deeper locking depth of 10.5 km. Similarly, excluding station GA18 in the southern profile results in a deeper locking depth estimate of 3.2 km compared with the 0.8 km obtained when including GA18 in the inversion. The 68 per cent confidence level ellipses shown in Figs 5(c) and (d) are elongated, showing a clear trade-off between slip rates and fault locking depths. As demonstrated in several studies, higher slip rates require deeper locking depths (e.g. Wright *et al.* 2001; Meade & Hager 2005; Smith-Konter *et al.* 2011). This correlation arises from the tight constraint on the near-field velocity gradient imposed by the dislocation model (see Wright *et al.* 2001,for details).

Finally, we compared our results with the slip rates and locking depths derived by Li *et al.* (2021) based on the implementation of Sentinel 1 burst-overlap interferometry (BOI) in the lands bordering the gulf (light orange curves in Figs 5a and b). Taken together, both results indicate shallower locking depths from north to south, towards the Red Sea rift. Our results further suggest that a very shallow locking depth or creeping is required in the southern part of the gulf to account for the low strain accumulation observed in this

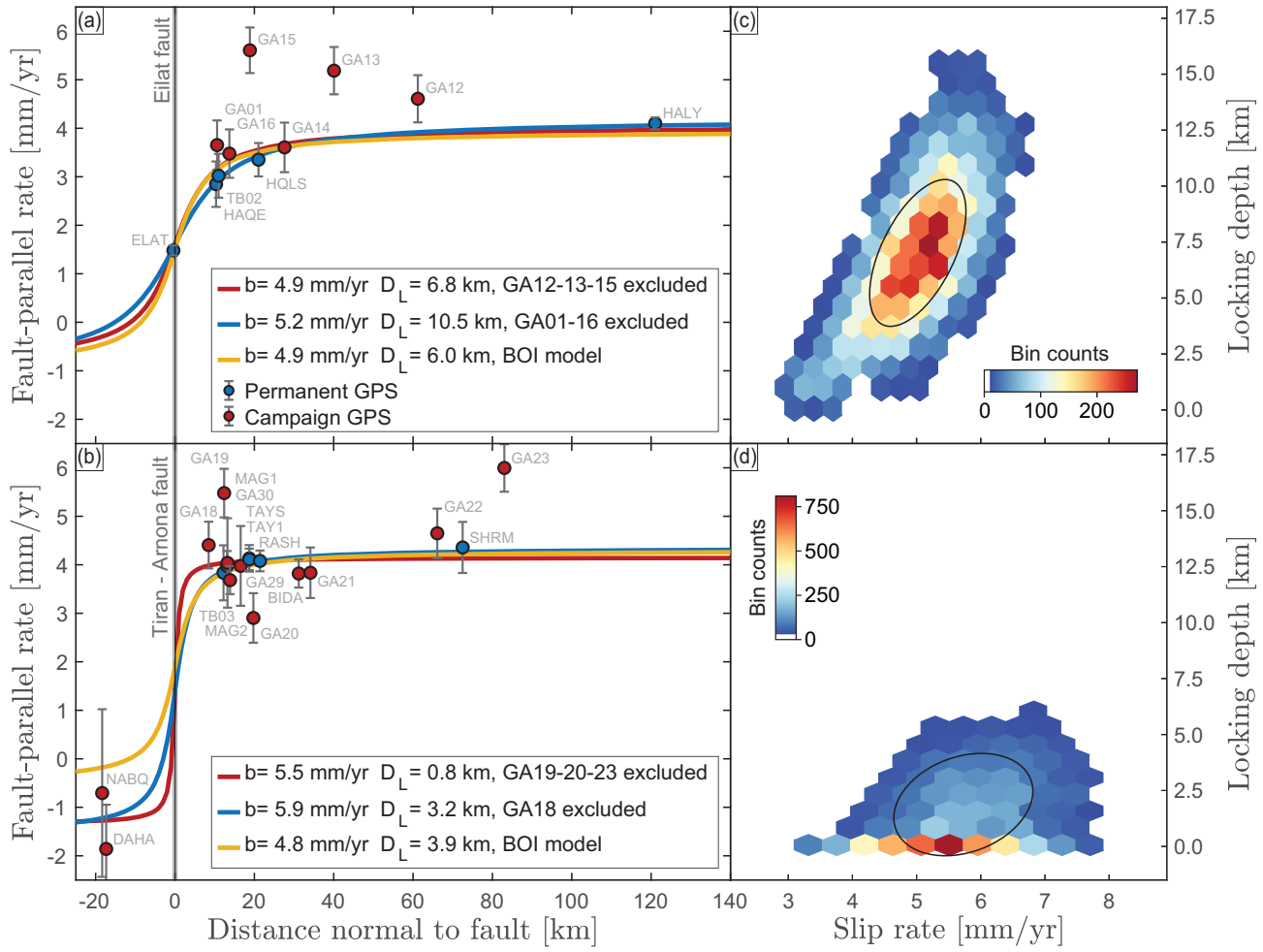

Figure 5. Observed fault-parallel velocities with 1σ uncertainties across the Eilat fault (panel a) and Tiran–Arnona faults (panel b) in comparison with predictions from elastic dislocation models in a Sinai-fixed reference frame. Panels (c) and (d) depict the results of the slip rate and locking depth inversions and 68 per cent confidence level ellipses. The red curve in both profiles represents the global minimum considering a, b and D_L as free parameters. Results from Li *et al.* (2021), based on BOI observations, are shown in light orange.

area. However, the current near-fault GPS data are insufficient to unambiguously discriminate between shallow locking and full creep scenarios along the southern fault segments. These results motivated us to implement a more complex model of strain accumulation, which not only considers fault-parallel motions but also allows for tensile motions and rigid block rotations.

5 BACK-SLIP MODEL

Interseismic deformation studies conducted further north along the DST in Israel, Jordan, Syria and Lebanon have shown that GPS-derived velocities can be well explained by rigid block movement bounded by a narrow deformation zone that accommodates the relative motion between them (e.g. Mahmoud *et al.* 2005; Reilinger *et al.* 2006; Gomez *et al.* 2007, 2020; Al Tarazi *et al.* 2011). This view is also supported by the distribution of instrumental and historical seismicity, which concentrates along the main fault strands of the DST fault system (Hofstetter *et al.* 2014). We thus next investigated whether the velocity field in the Gulf of Aqaba area can also be explained using a similar back-slip model.

We adopted the approach described by McCaffrey (2005, 2009) and defined two blocks representing the Sinai and Arabian plates. The boundary between them was modelled as a set of linear fault segments representing the main fault strands of the gulf mapped by Ben-Avraham (1985) and Ribot *et al.* (2021), with short relay faults connecting the segments (Figs 6 and 7). Model-predicted velocities result from superimposing linear rates due to block rotations and those associated with the back-slip motion applied on block boundaries, which are estimated following Okada (1985).

The number of near-fault GPS observations is insufficient to reliably invert for the locking fraction distribution along the fault segments within the gulf, even for sparse discretizations of the fault planes. Hence, we considered three forward back-slip model scenarios defining the locking fraction of the fault segments *a priori*. In the first scenario, we imposed full interseismic locking on all the faults in the gulf (Fig. 6a). In the second scenario, we considered creep on the Arnona fault and TF (Fig. 6b). Finally, in the third scenario, we imposed creep on the TF only (Fig. 7). Locked faults were modelled as near vertical extending down to 7 km, based on our best-fitting estimate across the Eilat fault. Creeping faults were modelled as free-slipping boundaries that do not produce any elastic strain. To evaluate the effect of implementing different fault geometries in our back-slip models, we ran an additional scenario assuming a dip angle of 65° for the Aragonese fault, as proposed by Baer

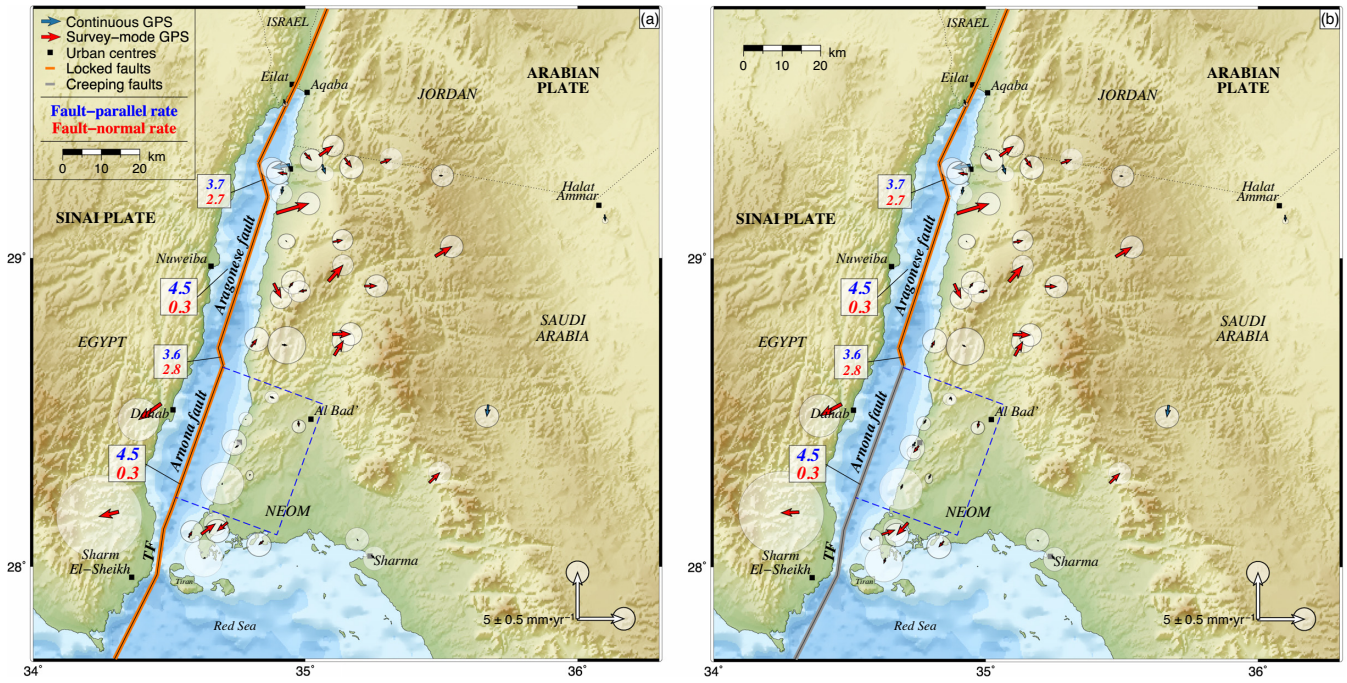

Figure 6. Panel (a) shows residual velocities after implementing the first back-slip model scenario assuming full interseismic locking on all the fault traces. Panel (b) shows the residuals obtained after implementing the second scenario assuming full creep along the Arnona fault and the TF. Orange and grey lines represent locked and creeping fault traces, respectively. Residual rates of seven near-fault stations within the blue dashed boxes are analysed in Fig. S6 in the Supporting Information.

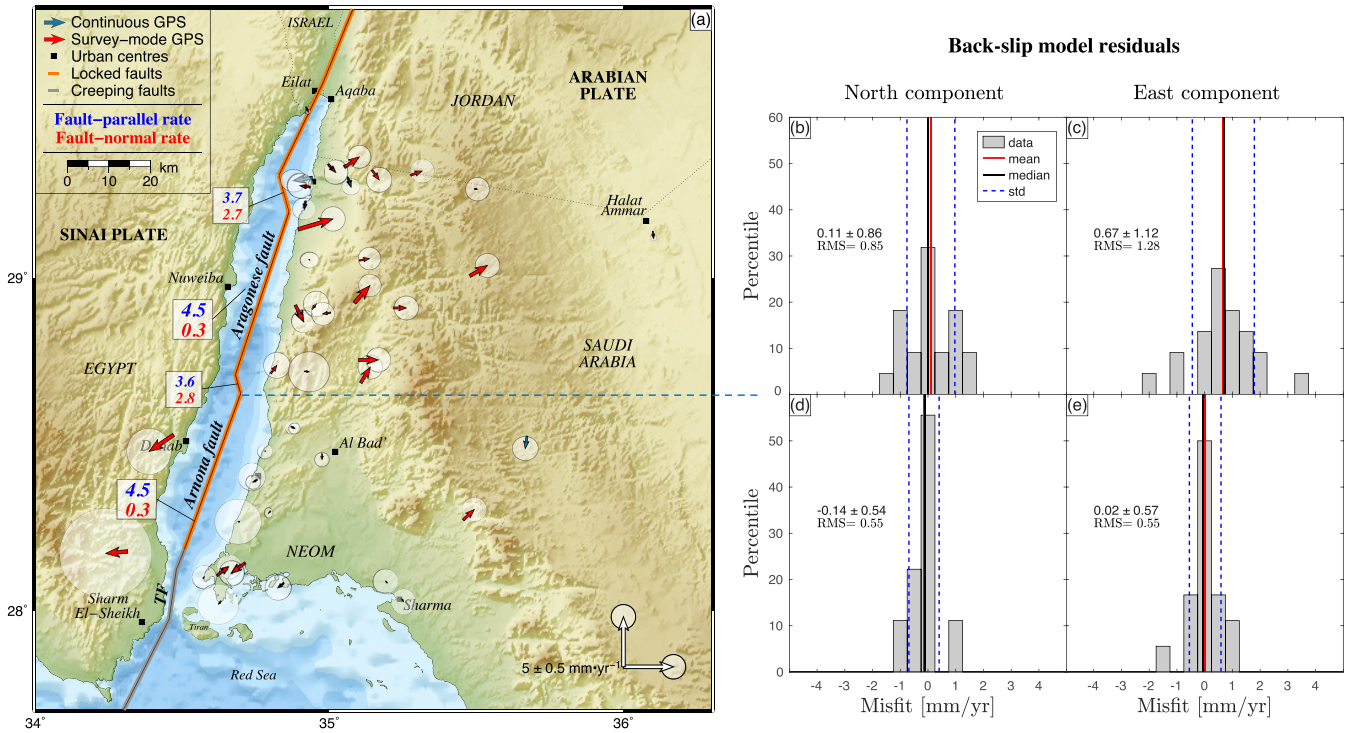

Figure 7. Residual velocity vectors after implementing the third back-slip model scenario (panel a), which assumes full creep on only the TF. Histograms of fault parallel and perpendicular residuals for the northern part of the gulf (north of the blue dashed line) are shown in panels (b) and (c) and for the southern part in panels (d) and (e), with both the bias and RMS values reported.

et al. (2008). By comparing the resulting back-slip model residuals with those obtained assuming a vertical fault (Fig. 7), we show that the variance difference is not large enough to be statistically significant, as depicted in Fig. S5 in the Supporting Information.

Considering that most stations in the gulf area have short time-series (<5 yr), we did not optimize for rotation parameters during the back-slip modelling. Instead, we defined the Arabia-Sinai Euler pole *a priori* using the Sinai-ITRF2014 Euler vector derived in this

study and the Arabia-ITRF2014 rotation pole reported by Altamimi *et al.* (2017). In this way, the back-slip applied on each locked fault in the gulf was determined by the Arabia-Sinai rotation pole (35.00° N, 8.78° E, $\omega = 0.105°\text{Ma}^{-1}$), assuming that no aseismic slip occurs during the interseismic period on those faults. Finally, we compared observed and back-slip predicted velocities in the gulf area and analysed the residual rates.

Our modelling results indicate that the coastal areas bordering the Arnona fault are undergoing strain accumulation. This is supported by the good fit to the data on the Arabian side of the gulf obtained by imposing full interseismic locking to the Arnona fault in the first model scenario (Fig. 6a) and the small but coherent southward residuals obtained in the second scenario, where creeping is assumed along the Arnona fault and TF (Fig. 6b). We analysed these residuals quantitatively, showing that when the Arnona fault is assumed to be fully locked, near-fault velocity residuals are close to zero (panels a and b in Fig. S6, Supporting Information). In contrast, full-creep on the Arnona fault leads to a systematic bias of ∼0.4 and ∼0.2 mm yr^{-1} in the north and east velocity components, respectively (panels c and d in Fig. S6, Supporting Information). We also noted that the fit to the data across TF degrades if this fault is assumed to be locked during the interseismic period. This observation suggests that creeping might be required to explain the low interseismic strain accumulation observed across this fault. We found that the best fit to the data is obtained by implementing scenario 3, which considers full locking along all the fault segments except TF, which is modelled as a creeping fault. Scenario 3 explains the interseismic strain accumulation observed across the Arnona fault and the full-plate rate exhibited by near-fault GPS stations across TF (see Fig. 7a).

Our results further suggest a fault-parallel slip rate of ∼ 4.5 mm yr^{-1} and a tensile component of ∼ 0.3 mm yr^{-1} along the main fault strands in the gulf, as determined from the relative plate motion (see Fig. 7a). The back-slip model succeeds in fitting 13 out of 17 GPS rates (76 per cent) within their 95 per cent confidence ellipses in the southern region of the gulf (east of the Arnona fault and TF traces). Nevertheless, our modelling results reveal an apparent reduction in the quality of the fit for most sites located in northern Gulf of Aqaba (east of the Aragonese fault trace), where only 12 out of 23 observations (52 per cent) were fitted within their 95 per cent confidence ellipses. Interestingly, residual velocities are not randomly distributed but are instead systematically directed towards the east–northeast on the Arabian side of the gulf. This observation led us to investigate in more detail the nature of these residuals and their spatial distribution. For this purpose, we estimated descriptive statistics of the misfits, discriminating between stations in the northern and southern regions of the gulf.

The misfit distributions depicted in Figs 7(b)–(e) quantitatively demonstrate that the magnitude of residual velocities differs between the northern and southern regions on the Arabian side of the gulf. Notably, the average magnitude of the east component of residual velocities in the northern area is about 0.7 mm yr^{-1}. This value contrasts with that observed east of the Arnona fault in the southern region of the gulf, where the east component of residual velocities is roughly zero. Similarly, but to a lesser extent, we observe a small discrepancy in the north component of residual velocities. The mean magnitude of the north component of residual velocities east of the Aragonese fault is 0.11 mm yr^{-1}, while the average value of the same velocity component observed east of the Arnona fault in the southern region of the gulf is −0.14 mm yr^{-1}. Our results thus suggest the existence of a left-lateral residual motion across the gulf that cannot be explained by block rotations and interseismic strain accumulation alone. These results drove us to study the potential influence of post-seismic transient motions caused by the 1995, M_w 7.2 Nuweiba earthquake in the lands bordering the gulf.

6 POST-SEISMIC MODELLING

Transient surface deformation has been systematically observed following large earthquakes spanning periods from months to decades (Scholz 2002). Three time-dependent mechanisms are most often tested to explain such deformation transients: Afterslip on and/or around the ruptured fault plane (e.g. Savage *et al.* 1994; Bürgmann *et al.* 1997), poroelastic rebound (e.g. Peltzer *et al.* 1996; Jónsson *et al.* 2003) and viscoelastic relaxation of the lower crust and upper mantle (e.g. Pollitz 1997; Freed & Bürgmann 2004). The last one is the only process capable of producing post-seismic deformation spanning both large spatial and long temporal scales (Vergnolle *et al.* 2003, and references therein). Despite considerable efforts aimed at elucidating the underlying nature of the mechanisms controlling post-seismic deformation, discriminating among them using geodetic measurements is challenging and is presently an active area of research (e.g. Jónsson 2008; Liu *et al.* 2020).

Considering the limited GPS measurements in the years following the 1995 Nuweiba earthquake, the data are insufficient to invert for rheological parameters. Hence, we set up a series of forward models to analyse the post-seismic surface deformation resulting from different lithospheric structures for the Gulf of Aqaba. For this purpose, we studied the viscoelastic relaxation following the methodology proposed by Wang *et al.* (2006) for a layered viscoelastic Earth model accounting for gravity effects. We used a simplified 1-D velocity model of the gulf area from Tang *et al.* (2016) to define a layered Earth structure consisting of a Burgers viscoelastic half-space underlying a 30 km thick elastic layer, representing the Earth's upper mantle and crust, respectively (see Figs 8b–d). We also considered a three-layer Earth structure consisting of a 30 km elastic upper crust underlain by a biviscous lower crust and upper mantle (see Fig. 8e). The source of the M_W 7.2 Nuweiba earthquake was modelled using the distributed slip model derived by Baer *et al.* (2008) from ERS-1 and ERS-2 Interferometric Synthetic Aperture Radar (InSAR) data (see Fig. 9).

We explored four model scenarios by varying the transient and steady-state viscosities of the Burgers solids. In the first three scenarios, the viscosity of the underlying half-space was set based on the best-fitting viscosity reported by Piersanti *et al.* (2001) for the Sinai-Suez area (∼ 10^{18} Pa · s). In the fourth scenario, we considered a thin crème brûlée rheological structure consisting of a 30 km elastic upper crust underlain by a biviscous lower crust and upper mantle. Following the considerations above, in scenario 1, we assigned values of 1×10^{18} and 1×10^{19} Pa · s to the transient (η_K) and steady-state (η_M) viscosities, respectively. In scenario 2, we fixed η_K to 2×10^{18} Pa · s and η_M to 2×10^{19} Pa · s. In scenario 3, we considered a higher transient viscosity of 1×10^{19} Pa · s and a steady-state viscosity of 1×10^{20} Pa · s. Finally, in scenario 4, we defined steady-state viscosities of 2×10^{18} and 4×10^{19} Pa · s for the lower crust and upper mantle, respectively (transient/steady-state viscosity = 0.1). We held fixed the ratio between effective and unrelaxed shear modulus (α) to a value of 0.5 in the first three scenarios, and 0.7 in the last model (see below).

For each model scenario, we computed time-series of post-seismic displacements for the period spanning from the origin time

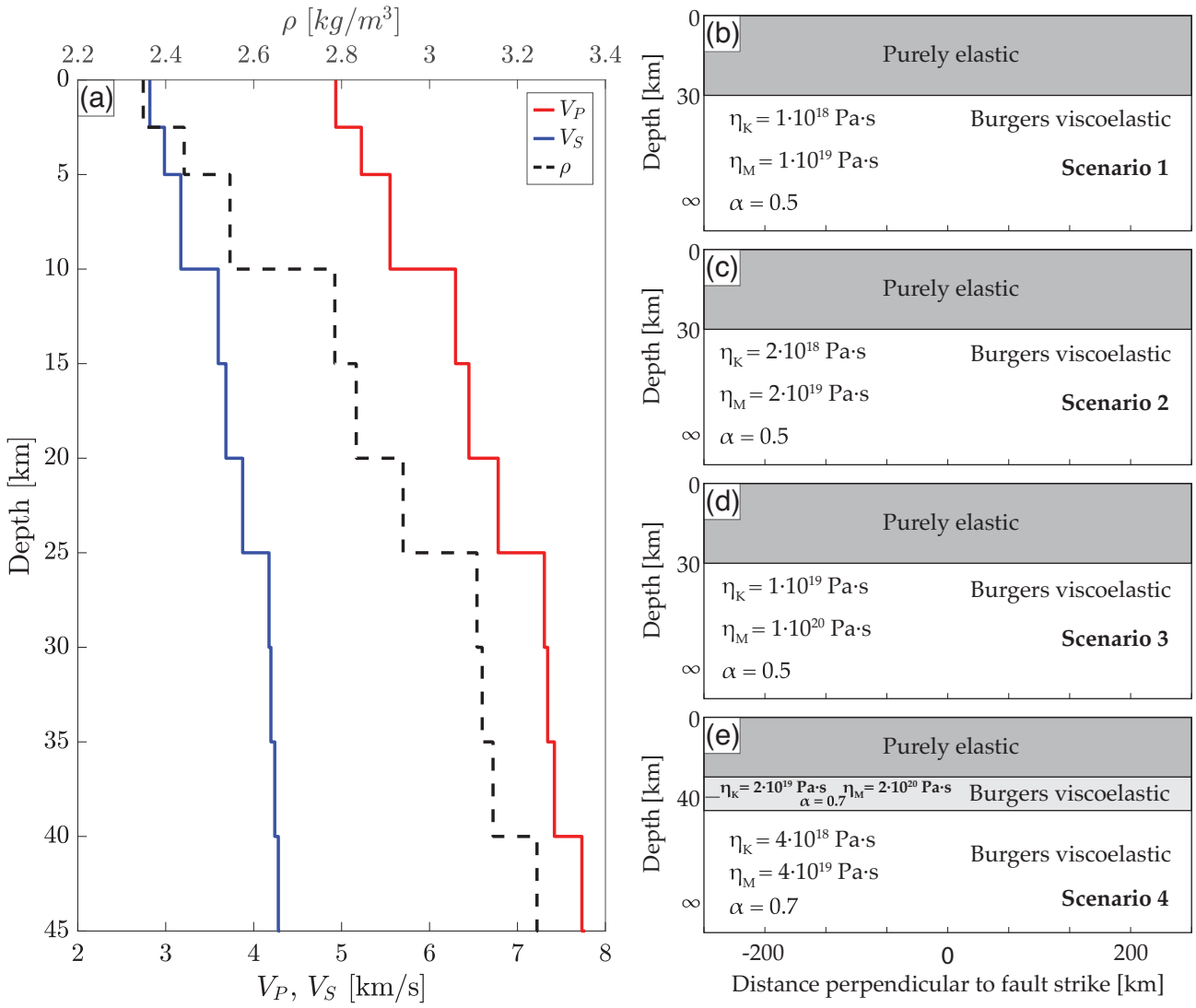

Figure 8. Panel (a) shows the simplified 1-D layered Earth model of the Gulf of Aqaba (adapted from Tang *et al.* 2016). Panels (b)–(e) are schematic representation of the lithosphere for model scenarios 1–4, respectively. Viscoelastic parameters of the Kelvin and Maxwell elements are also given for each scenario: η_K is the transient viscosity (dashpot of the Kelvin solid) and η_M represents the steady-state viscosity (dashpot of the Maxwell fluid). α corresponds to the ratio between effective and unrelaxed shear modulus $\frac{\mu_K}{\mu_K+\mu_M}$. The unrelaxed shear modulus (μ_M) can be derived from the values of *S*-wave velocities (V_s) and densities (ρ) provided in panel (a).

of the 1995 Nuweiba earthquake to the year 2020. Post-seismic velocities were then derived from the average displacement rate over the observation period of each GPS station. As can be seen in Fig. 9, model scenarios implementing lower transient and steady-state viscosities result in slightly higher post-seismic rates compared with those including higher viscosities. The pattern of modelled post-seismic velocities in all four cases is similar and shows left-lateral motion, which agrees with the coseismic slip prescribed in the finite-fault model. However, unlike the modelled interseismic velocities, the predicted post-seismic deformation fields exhibit maximum fault-parallel velocities about 30 km away from the fault trace, with lower rates next to the fault and in the far-field.

To determine whether the back-slip model residuals shown in Fig. 7 can be explained by post-seismic transient motions from the Nuweiba earthquake, we estimated the misfits resulting from subtracting modelled post-seismic rates from the block model residuals. Fig. 10(a) depicts the misfit vectors obtained for the four post-seismic model scenarios considered in our study. As done in the back-slip model, we discriminated between GPS stations located in the northern and southern regions adjacent to the gulf on the Arabian plate. The misfit distributions and RMS values for each post-seismic model are shown in Figs 10(b)–(e).

Overall, the lowest RMS misfits east of the Aragonese fault were obtained by implementing model scenario 2 (green vectors in Fig. 10a). Modelled post-seismic velocities in the north (east of Aragonese fault trace) lead to a reduction in the RMS misfit by ∼11 per cent and ∼1 per cent of the east and north velocity components, respectively. In contrast, the quality of the fit in the southern region of the gulf (east of the Arnona fault and TF traces) degraded by 4 per cent and 41 per cent in east and north velocity components, respectively. The reduction in the quality of the fit in this area is due to northwestward modelled post-seismic velocities, which are not observed in the block-model residuals. As shown in Fig. 7, GPS-derived velocities are well-fitted by the back-slip model in the gulf's southern region located east of the Arnona fault and

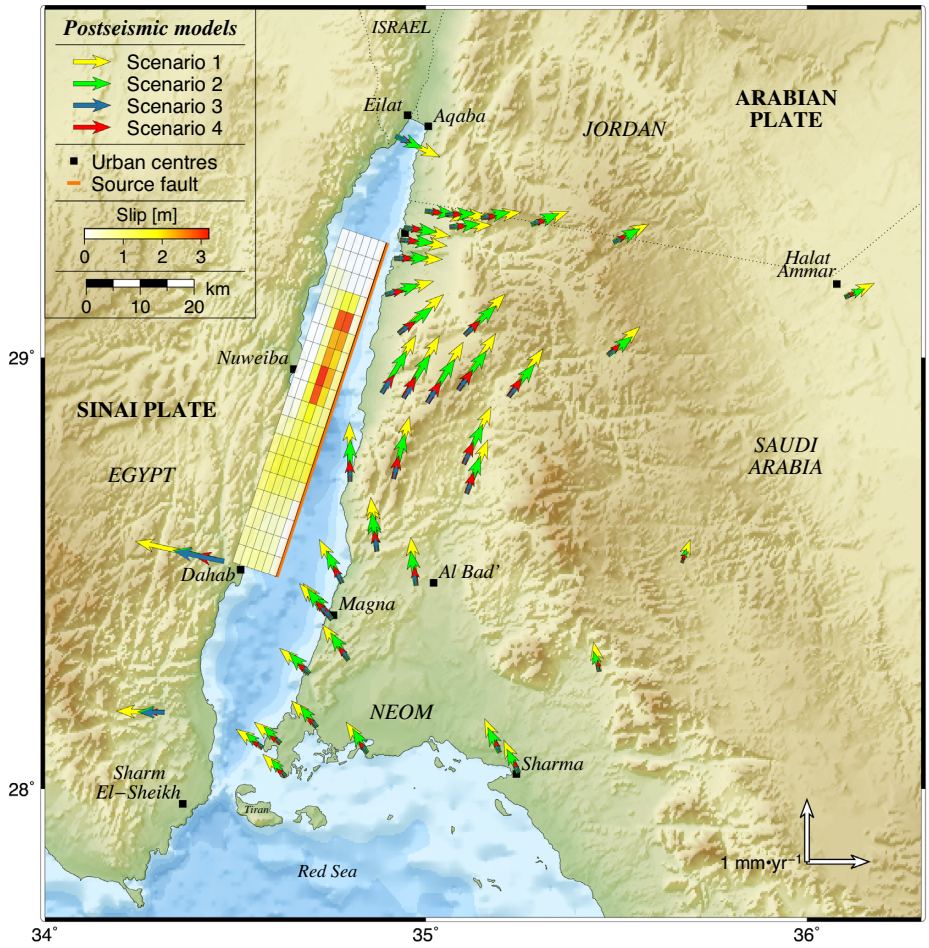

Figure 9. Modelled post-seismic velocities computed at the location of GPS stations in the study area. Yellow, green, blue and red vectors represent modelled post-seismic velocities for scenarios 1, 2, 3 and 4, respectively. Post-seismic rates were estimated for the observation period at each GPS station (see Fig. S1, Supporting Information for details). The colour-coded grid represents the finite-source model of the Nuweiba earthquake derived by Baer *et al.* (2008). Note the change in velocity scale from previous figures.

TF. Hence, the consideration of any additional post-seismic signal in the southern region of the gulf results in a degradation of the fit.

Our results suggest that modelled post-seismic velocities induced by the 1995, M_W 7.2 Nuweiba earthquake explain part of the left-lateral residual motion observed in the lands bordering the gulf. However, the forward models fail to satisfactorily reproduce the magnitudes of the residual velocity field by underestimating somewhat the back-slip model residuals in the northeast of the gulf while overshooting observed residuals to the southeast.

7 DISCUSSION

Previous estimates of the relative motion between the Sinai and Arabian plates along the Gulf of Aqaba relied on sparse observations at a limited number of GPS sites located on each side of the gulf (e.g. Mahmoud *et al.* 2005; Reilinger *et al.* 2006; ArRajehi *et al.* 2010; Gomez *et al.* 2020). However, the establishment of 27 survey-mode sites in 2014 and the rapid expansion of permanent geodetic networks in Saudi Arabia during the last decade have allowed us to derive an updated GPS velocity field of this region.

By implementing an elastic half-space model, we derived a slip rate of $4.9^{+0.9}_{-0.6}$ mm yr^{-1} and a locking depth of $6.8^{+3.5}_{-3.1}$ km across the Eilat fault. We also estimated a slip rate of $5.5^{+1.3}_{-0.9}$ mm yr^{-1} and a locking depth of $0.8^{+3.4}_{-0.8}$ km further south across the Arnona fault and TF (see red curves in Figs 5a and b). While the slip rates derived here agree with previous studies, locking depth estimates are shallower than those reported along the Wadi Arabah fault north of the gulf, which range between 12 and 20 km (e.g. Le Béon *et al.* 2008; Sadeh *et al.* 2012; Masson *et al.* 2015; Hamiel *et al.* 2018a; Gomez *et al.* 2020). Further south, stations' rates show little evidence of strain accumulation despite their proximity to the TF. This pattern agrees with a very shallow locking depth, which might indicate potential creep along this fault segment (see Fig. 5b).

To evaluate the impact of outliers in the slip rate and locking depth inversions, we ran additional tests considering all the stations in the profiles including stations with anomalous rates. Inversions including all the GPS stations in the northern profile yielded a slip rate of $6.7^{+0.7}_{-0.7}$ mm yr^{-1} and a locking depth of $8.8^{+2.2}_{-2.2}$ km. Further south, across the Arnona fault and TF, this test resulted in a slip rate of $5.9^{+1.3}_{-0.7}$ mm yr^{-1} and a locking depth of $2.5^{+3.2}_{-2.2}$ km. Our results thus suggest that the slip rates seem to be more affected by the outlier rates in the mid- and far-field than the locking depths (see Fig. S4, Supporting Information). Although the slip rates and locking depths for the southern profile are not as well constrained as for the northern profile, our modelling results show that the buried screw dislocation model provides consistent locking depth estimates even in the presence of the outliers, indicating shallower locking depths in the south.

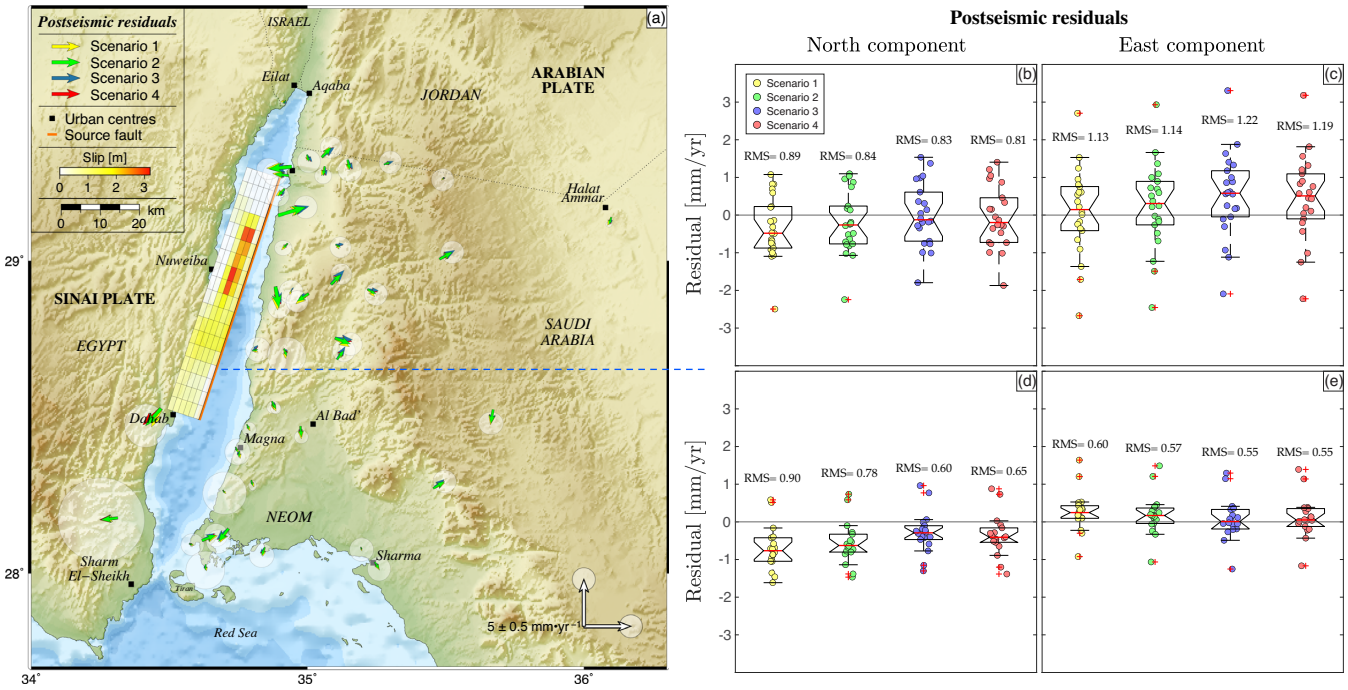

Figure 10. Residual velocities after implementing four post-seismic model scenarios discussed in the text, with the orange line delineating the 1995 coseismic fault rupture of the Aragonese fault (after Baer *et al.* 2008). For visualization purpose, 95 per cent confidence ellipses are shown only for the best-fitting post-seismic model (scenario 2). The contrast between the residuals of stations in the northern half of the gulf (East of the Aragonese fault trace) and South (East of the Arnona fault trace) is illustrated in panels (b)–(e), with notched boxes enclosing data within 25th and 75th percentiles. For each scenario, the median of the misfit distribution is shown as a solid red line and whiskers extend to the most extreme data points not considered as outliers, which are represented by the red crosses.

Previous geophysical studies conducted along the on-land portion of the DST and its offshore extension in the Gulf of Aqaba indicate a systematic thinning of the lithosphere towards the Red Sea (e.g. Ginzburg *et al.* 1979; Ben-Avraham 1985; Mohsen *et al.* 2006; El Khrepy *et al.* 2016a). Ben-Avraham (1985) conducted gravity, magnetic and seismic surveys in the gulf, and proposed a thinner crust in its southern region. This observation agrees with earlier investigations indicating higher heat flow values and gradual crustal thinning towards the south (e.g. Ginzburg *et al.* 1979; Ben-Avraham & Von Herzen 1987). Similarly, tomographic inversions and *S*-receiver function studies revealed that the lithospheric thickness decreases from 80 km north of the Dead Sea to 65 km in the Gulf of Aqaba, indicating stronger asthenospheric upwelling in the south (Mohsen *et al.* 2006; El Khrepy *et al.* 2016a). More recently, Li *et al.* (2021) implemented along-track Sentinel-1 BOI time-series analysis and reported decreasing locking depths from 15.9 ± 1.9 km of the Wadi Arabah fault to only 3.9 ± 1.5 km in the southern part of the Gulf of Aqaba. Hence, the locking depth reduction from north to south along the Wadi Arabah and faults within the gulf might be explained by progressive crustal thinning towards the Red Sea.

We estimated a slip rate of $\sim$ 4.5 mm yr^{-1} along the main fault segments in the gulf based on a forward back-slip model, which implemented the Arabia-Sinai Euler pole derived in this study. This estimate is lower than the best-fitted inverted in our screw dislocation models, and could be attributed to potential internal deformation or fragmentation of the Sinai plate, as has been reported in recent studies (e.g. Gomez *et al.* 2020). The present-day slip rate derived from geodetic data in the gulf area agrees well with the long-term geological estimates along the southern on-land portion of the DST, which converge to an average value of 5 ± 1 mm yr^{-1} (e.g. Le Béon *et al.* 2010, 2012). We can thus assume that the present-day slip rate has remained relatively constant over the last millennium. Based on this assumption, the Eilat and Arnona faults have accumulated significant moment since the last historical earthquakes that struck the gulf area in 1212 AD and 1588 AD (e.g. Ambraseys 2009; Agnon 2014; Klinger *et al.* 2015; Lefevre *et al.* 2018).

We estimated the slip deficit and moment accumulation rate on the major strike-slip faults in the gulf, assuming that they are fully locked during the interseismic period. We also considered an additional scenario assuming that the TF in the southern region of the gulf creeps aseismically. Considering that the 1212 AD and 1588 AD earthquakes cannot be unambiguously assigned to specific fault traces within the gulf, we tested both as potential last earthquakes on the Eilat and Arnona faults. For this purpose, we evaluated lower and upper bound estimates based on the fault kinematic parameters derived in this research and previous investigations along the southern on-land portion of the DST, corresponding to slip rates ranging between 4.4 and 5.2 mm yr^{-1} (e.g. Mahmoud *et al.* 2005; Reilinger *et al.* 2006; Le Béon *et al.* 2008; ArRajehi *et al.* 2010; Al Tarazi *et al.* 2011; Sadeh *et al.* 2012; Masson *et al.* 2015; Hamiel *et al.* 2016, 2018; Gomez *et al.* 2020). For the locking depths, we considered the lower and upper bounds from the 1σ uncertainty derived in the gulf's northern region, corresponding to locking depths ranging between 4 and 10 km (see Fig. 5a).

Table 1 summarizes the parameters considered in our calculations (fault length L, locking depth L_D and slip rate $\dot{u}$) as well as estimates of the slip deficit u, geodetic moment M_0, moment accumulation rate $\dot{M}_0$ and the associated moment magnitude M_W for each fault segment, which was computed based on the scaling regression by Hanks & Kanamori (1979). The slip deficit and moment accumulation rates estimated for the Eilat and Arnona faults suggest that impending earthquakes could reach M_W 6.7–7.3, assuming that the

Table 1. Fault parameters and estimated earthquake potential for the main strike-slip fault segments in the Gulf of Aqaba.

Fault	L [km]	L_D [km]	$\dot{u}$ [mm yr^{-1}]	Last EQ	u [m]	M_0 [Nm]	$\dot{M}_0$ [Nm yr^{-1}]	M_W
Eilat	59	4	4.4	1212	3.56	2.517×10^{19}	3.115×10^{16}	6.9
		10	5.2		4.20	7.437×10^{19}	9.204×10^{16}	7.2
	59	4	4.4	1588	1.90	1.346×10^{19}	3.115×10^{16}	6.7
		10	5.2		2.25	3.976×10^{19}	9.204×10^{16}	7.0
Aragonese	53	4	4.4	1995	0.11	6.996×10^{17}	2.798×10^{16}	5.9
		10	5.2		0.13	2.067×10^{18}	8.268×10^{16}	6.2
Arnona	83	4	4.4	1212	3.56	3.541×10^{19}	4.382×10^{16}	7.0
		10	5.2		4.20	1.046×10^{20}	1.295×10^{17}	7.3
	83	4	4.4	1588	1.90	1.893×10^{19}	4.382×10^{16}	6.8
		10	5.2		2.25	5.593×10^{19}	1.295×10^{17}	7.1
Tiran	50	Creep	4.4	–	–	–	–	–
			5.2					

moment accumulated since the last known historical or instrumental earthquakes ('Last EQ') would be released by an earthquake on each fault strand. Estimates of the slip deficit and moment accumulated on the Aragonese fault are much smaller, as expected, considering that this fault strand ruptured during the 1995 M_W 7.2 Nuweiba earthquake (Klinger *et al.* 1999; Shamir *et al.* 2003; Hofstetter 2003; Baer *et al.* 2008; Ribot *et al.* 2021). Our results thus agree with previous studies suggesting that the Eilat and Arnona faults might be in a late stage of their current interseismic period (e.g. Hamiel *et al.* 2018a; Kanari *et al.* 2020; Ribot *et al.* 2021).

Our modelling results reveal a residual left-lateral motion across the gulf that cannot be resolved by standard models of interseismic strain accumulation (Figs 7 and 10). The nature of these velocity residuals is a subject of debate. While some studies speculate that they could be caused by interseismic elastic strain accumulation along the faults bounding the pull-apart basins in the Gulf of Aqaba (e.g. Pietrantonio *et al.* 2016)), others point out that they could be due to post-seismic motions induced by the 1995 Nuweiba Earthquake (e.g. Piersanti *et al.* 2001; Pe'eri *et al.* 2002; Riguzzi *et al.* 2006; Gomez *et al.* 2020).

We consider four possible explanations for the left-lateral residual motion observed across the gulf. The first possibility is that anomalous misfits are due to poor Euler vector parameters for the Sinai subplate relative to ITRF2014. However, this explanation is not supported by the velocity field obtained for stations of the GIL network in Israel, which exhibit residual velocities close to zero, evidencing the robustness of the Euler vector parameters derived in our study (see Table S2 and Fig. S2, Supporting Information). A second possibility is that the resulting misfits reflect the difference in temporal baselines between stations situated in the northern and southern regions of the gulf, as shown in Fig. S1, Supporting Information. This hypothesis might explain the small residuals obtained for stations with longer time-series located east of the Arnona fault (sites MAG1, MAG2 and BIDA, RASH, TAYS, TAY1, TB03, SHRM). Nevertheless, it fails to explain the systematic nature of residual motions.

A third hypothesis is that the relative motion between the Arabian and Sinai plates along the Gulf of Aqaba is accommodated by a wide deformation zone extending up to ∼50 km across both plates. Several studies have identified two shear belts composed of anastomosing faults on both sides of the gulf (e.g. Freund *et al.* 1970; Bartov *et al.* 1980; Eyal *et al.* 1981; Garfunkel 1981; Lyberis 1988). Earlier investigations indicate that these faults were active primarily during the first slip stages along the DST and do not affect post-Miocene stratigraphic units (e.g. Bartov *et al.* 1980; Eyal *et al.* 1981; Garfunkel 1981). A more recent study reported small-scale normal faults affecting post-Miocene strata and Pleistocene coral terraces, indicating ENE-WSW extension (Bosworth *et al.* 2017). However, the seismicity recorded in the gulf area shows that most earthquakes concentrate along the gulf itself and the coastal plains (e.g. Ben-Avraham *et al.* 1979; Bartov *et al.* 1980, Fig. 2), suggesting that recent deformation is confined to those areas.

Finally, the systematic left-lateral residual signal could reflect ongoing post-seismic deformation caused by the Nuweiba Earthquake. A recent study by Liu *et al.* (2020) found that the lower crust exhibits ductility at decadal time scales, and thus post-seismic transient motions may be larger and more enduring than previously thought. As noted by Piersanti *et al.* (2001), the motion of stations DAHA and NABQ on the Sinai side of the gulf is puzzling, considering that they exhibit motions that are opposite to the direction predicted by interseismic models of strain accumulation (see Fig. 3). Similarly, the updated velocity field presented in this study allowed us to quantitatively identify northeastward residuals east of the Aragonese and Eilat faults, which agree with the overall pattern of modelled post-seismic rates.

We speculate that the misfit between the magnitudes of theoretical post-seismic motions and residuals from the back-slip model may arise from structural and rheological complexities in the gulf (e.g. Ben-Avraham 1985; El Khrepy *et al.* 2016a, b), which were not considered in our forward models. Therefore, post-seismic motions and relaxation times could exhibit significant spatial variations depending on the lithospheric structure in different regions of the gulf and the slip distribution used to model the Nuweiba earthquake.

8 CONCLUSIONS

The establishment of 27 survey-mode GPS stations in 2014 and the analysis of up to 19 yr of geodetic observations on the Arabian and Sinai-Levant plates allowed us to derive an updated crustal motion velocity field of the lands bordering the Gulf of Aqaba. By implementing an elastic interseismic model, we derived a slip rate of $4.9^{+0.9}_{-0.6}$ mm yr^{-1} and a locking depth of $6.8^{+3.5}_{-3.1}$ km across the Eilat fault in the gulf's northern region. Our modelling results suggest that either a shallow locking depth or creeping might be required to explain the low interseismic strain accumulation observed in the gulf's southern region across TF. We identified a systematic left-lateral residual motion across the gulf, characterized by

northeastward residuals east of the Aragonese fault and southwestward residuals west of the Arnona fault. We postulate that postseismic transient motions caused by the 1995, M_W 7.2 Nuweiba earthquake could potentially explain these misfits. Estimates of the geodetic moment accumulated on the Eilat and Arnona faults since the last historical earthquakes that struck the gulf area in 1212 AD and 1588 AD indicate that impending earthquakes on these faults could potentially reach M_W 6.7–7.3, posing a significant hazard to the urban centres along the gulf coast. Future studies would benefit from incorporating additional GPS stations on the Sinai side of the gulf, refined slip models of the Nuweiba earthquake and more detailed information about historical earthquakes in the gulf region.

ACKNOWLEDGEMENTS

We thank Hannes Vasyura-Bathke, Joël Ruch, Jon Harrington, Samer Almashharawi, Mohammad Youssof, Laura Parisi, Adel Sherif and the students of the 2015 Seismotectonics course at King Abdullah University of Science and Technology (KAUST) for the help with the GPS fieldwork campaigns. We also thank the Saudi Geological Survey (SGS) and King Abdulaziz City for Science and Technology (KACST) for providing the continuous GPS data from the gulf's stations. Maps were generated using the Generic Mapping Tools, Version 5.4.5 (Wessel *et al.* 2013, https://www.generic-mapping-tools.org). This research was supported by KAUST, under award number OSR-2016-CRG5-3027.

DATA AVAILABILITY

The GPS data underlying this article will be made available on the UNAVCO archive, at https://www.unavco.org/data/dai/.

REFERENCES

Agnon, A., 2014. Pre-instrumental earthquakes along the dead sea rift, in *Dead Sea Transform Fault System: Reviews,* pp. 207–261, Springer.

Al Tarazi, E., Abu Rajab, J., Gomez, F., Cochran, W., Jaafar, R. & Ferry, M., 2011. GPS measurements of near-field deformation along the southern Dead Sea Fault System: GPS along the southern Dead Sea Fault, *Geochem. Geophys. Geosyst.,* **12**(12) doi:10.1029/2011GC003736.

Alamri, A. M., Schult, F. R. & Bufe, C. G., 1991. Seismicity and aeromagnetic features of the Gulf of Aqaba (Elat) Region, *J. geophys. Res.: Solid Earth,* **96**(B12), 20179–20185.

Altamimi, Z., Métivier, L., Rebischung, P., Rouby, H. & Collilieux, X., 2017. ITRF2014 plate motion model, *Geophys. J. Int.,* **209**(3), 1906–1912.

Ambraseys, N., 2009. *Earthquakes in the Mediterranean and Middle East: A Multidisciplinary Study of Seismicity up to 1900,* Cambridge University Press.

ArRajehi, A. *et al.*, 2010. Geodetic constraints on present-day motion of the Arabian Plate: implications for Red Sea and Gulf of Aden rifting: Arbabia plate motion, *Tectonics,* **29**(3) , doi:10.1029/2009TC002482.

Baer, G., Funning, G. J., Shamir, G. & Wright, T. J., 2008. The 1995 November 22, Mw 7.2 Gulf of Elat earthquake cycle revisited, *Geophys. J. Int.,* **175**(3), 1040–1054.

Bar, M., Kolodny, Y. & Bentor, Y., 1974. Dating faults by fission track dating of epidotes—an attempt, *Earth planet. Sci. Lett.,* **22**(2), 157–162.

Bartov, Y., Steinitz, G., Eyal, M. & Eyal, Y., 1980. Sinistral movement along the Gulf of Aqaba — its age and relation to the opening of the Red Sea, *Nature,* **285,** 220, doi: 10.1038/285220a0.

Becker, J. *et al.*, 2009. Global bathymetry and elevation data at 30 arc seconds resolution: Srtm30_plus, *Mar. Geod.,* **32**(4), 355–371.

Ben-Avraham, Z., 1985. Structural framework of the Gulf of Elat (Aqaba), Northern Red Sea, *J. geophys. Res.: Solid Earth,* **90**(B1), 703–726.

Ben-Avraham, Z. & Von Herzen, R. P., 1987. Heat flow and continental breakup: the gulf of elat (aqaba), *J. geophys. Res.: Solid Earth,* **92**(B2), 1407–1416.

Ben-Avraham, Z. & Zoback, M. D., 1992. Transform-normal extension and asymmetric basins: an alternative to pull-apart models, *Geology,* **20**(5), 423–426.

Ben-Avraham, Z., Almagor, G. & Garfunkel, Z., 1979. Sediments and structure of the Gulf of Elat (Aqaba)—Northern Red Sea, *Sediment. Geol.,* **23**(1-4), 239–267.

Ben-Avraham, Z. *et al.*, 2012. Structural styles along the Dead Sea Fault, in *Regional Geology and Tectonics: Phanerozoic Passive Margins, Cratonic Basins and Global Tectonic Maps,* pp. 616–633, Elsevier , doi:10.1016/B978-0-444-56357-6.00016-0.

Bock, Y. *et al.*, 1997. Southern california permanent gps geodetic array: continuous measurements of regional crustal deformation between the 1992 landers and 1994 northridge earthquakes, *J. geophys. Res.: Solid Earth,* **102**(B8), 18013–18033.

Bos, M. S., Fernandes, R. M. S., Williams, S. D. P. & Bastos, L., 2013. Fast error analysis of continuous gnss observations with missing data, *J. Geod.,* **87**(4), 351–360.

Bosworth, W., Montagna, P., Pons-Branchu, E., Rasul, N. & Taviani, M., 2017. Seismic hazards implications of uplifted pleistocene coral terraces in the gulf of aqaba, *Sci. Rep.,* **7**(1), 1–13.

Bürgmann, R., Segall, P., Lisowski, M. & Svarc, J., 1997. Postseismic strain following the 1989 loma prieta earthquake from gps and leveling measurements, *J. geophys. Res.: Solid Earth,* **102**(B3), 4933–4955.

Dong, D., Herring, T. A. & King, R. W., 1998. Estimating regional deformation from a combination of space and terrestrial geodetic data, *J. Geod.,* **72**(4), 200–214.

Dziewonski, A., Chou, T.-A. & Woodhouse, J. H., 1981. Determination of earthquake source parameters from waveform data for studies of global and regional seismicity, *J. geophys. Res.: Solid Earth,* **86**(B4), 2825–2852.

Ekström, G., Nettles, M. & Dziewoński, A., 2012. The global cmt project 2004–2010: centroid-moment tensors for 13,017 earthquakes, *Phys. Earth planet. Inter.,* **200,** 1–9.

El-Aal, A. E.-A. K. A. & Badreldin, H., 2016. Seismological aspects of the 27 June 2015 gulf of aqaba earthquake and its sequence of aftershocks, *J. Seismol.,* **20**(3), 935–952.

El-Isa, Z. H., Merghelani, H. M. & Bazzari, M. A., 1984. The Gulf of Aqaba earthquake swarm of 1983 January-April, *Geophys. J. Int.,* **78**(3), 711–722.

El Khrepy, S., Koulakov, I., Al-Arif, N. & Petrunin, A. G., 2016. *Seismic Structure beneath the Gulf of Aqaba and Adjacent Areas based on the Tomographic Inversion of Regional Earthquake Data,* Universitätsbibliothek Johann Christian Senckenberg.

El Khrepy, S., Koulakov, I. & Al-Arifi, N., 2016. Crustal and uppermost mantle structure beneath the continental rifting area of the gulf of suez from earthquake tomography, *Tectonophysics,* **668,** 92–104.

Elias, A. *et al.*, 2007. Active thrusting offshore Mount Lebanon: source of the tsunamigenic A.D. 551 Beirut-Tripoli earthquake, *Geology,* **35**(8), 755–758.

Eyal, M., Eyal, Y., Bartov, Y. & Steinitz, G., 1981. The tectonic development of the western margin of the Gulf of Elat (Aqaba) rift, *Tectonophysics,* **80**(1-4), 39–66.

Freed, A. M. & Bürgmann, R., 2004. Evidence of power-law flow in the mojave desert mantle, *Nature,* **430**(6999), 548.

Freund, R. *et al.*, 1970. The shear along the dead sea rift, *Phil. Trans. R. Soc. Lond., A.* 107–130.

Garfunkel, Z., 1981. Internal structure of the Dead Sea leaky transform (rift) in relation to plate kinematics, *Tectonophysics,* **80**(1–4), 81–108.

Ginzburg, A., Makris, J., Fuchs, K., Prodehl, C., Kaminski, W. & Amitai, U., 1979. A seismic study of the crust and upper mantle of the jordan-dead sea rift and their transition toward the mediterranean sea, *J. geophys. Res.: Solid Earth,* **84**(B4), 1569–1582.

Gomez, F. *et al.*, 2007. Global Positioning System measurements of strain accumulation and slip transfer through the restraining bend along the Dead Sea fault system in Lebanon, *Geophys. J. Int.,* **168**(3), 1021–1028.

Gomez, F., Cochran, W. J., Yassminh, R., Jaafar, R., Reilinger, R., Floyd, M., King, R. W. & Barazangi, M., 2020. Fragmentation of the Sinai Plate indicated by spatial variation in present-day slip rate along the Dead Sea Fault System, *Geophys. J. Int.,* **221**(3), 1913–1940.

Hamiel, Y. & Piatibratova, O., 2019. Style and distribution of slip at the margin of a pull-apart structure: geodetic investigation of the southern dead sea basin, *J. geophys. Res.: Solid Earth,* **124**(11), 12023–12033.

Hamiel, Y., Piatibratova, O. & Mizrahi, Y., 2016. Creep along the northern Jordan Valley section of the Dead Sea Fault, *Geophys. Res. Lett.,* **43**(6), 2494–2501.

Hamiel, Y., Masson, F., Piatibratova, O. & Mizrahi, Y., 2018a. GPS measurements of crustal deformation across the southern Arava Valley section of the Dead Sea Fault and implications to regional seismic hazard assessment, *Tectonophysics,* **724-725,** 171–178.

Hamiel, Y., Piatibratova, O., Mizrahi, Y., Nahmias, Y. & Sagy, A., 2018b. Crustal Deformation across the Jericho Valley Section of the Dead Sea Fault as resolved by detailed field and geodetic observations, *Geophys. Res. Lett.,* **45**(7), 3043–3050.

Hanks, T. C. & Kanamori, H., 1979. A moment magnitude scale, *J. geophys. Res.: Solid Earth,* **84**(B5), 2348–2350.

Heimann, A. & Ron, H., 1987. Young faults in the hula pull-apart basin, central dead sea transform, *Tectonophysics,* **141**(1–3), 117–124.

Herring, T., King, R. & McClusky, S., 2018. *Introduction to gamit/globk, Release 10.7,* Massachusetts Institute of Technology, Cambridge, MA.

Hofstetter, A., 2003. Seismic observations of the 22/11/1995 Gulf of Aqaba earthquake sequence, *Tectonophysics,* **369**(1–2), 21–36.

Hofstetter, A., Dorbath, C. & Dorbath, L., 2014. Instrumental data on the seismic activity along the dead sea transform, in *Dead Sea Transform Fault System: Reviews,* pp. 263–278, Springer , doi:10.1007/978-94-017-8872-4_9.

Joffe, S. & Garfunkel, Z., 1987. Plate kinematics of the circum Red Sea—a re-evaluation, *Tectonophysics,* **141**(1–3), 5–22.

Jónsson, S., 2008. Importance of post-seismic viscous relaxation in southern iceland, *Nat. Geosci.,* **1**(2), 136–139.

Jónsson, S., Segall, P., Pedersen, R. & Björnsson, G., 2003. Post-earthquake ground movements correlated to pore-pressure transients, *Nature,* **424**(6945), 179.

Kagan, E., Stein, M., Agnon, A. & Neumann, F., 2011. Intrabasin paleoearthquake and quiescence correlation of the late holocene dead sea, *J. geophys. Res.: Solid Earth (1978–2012),* **116**(B4) , doi:10.1029/2010JB007452.

Kanari, M., *et al.*, 2020. Seismic potential of the dead sea fault in the northern gulf of aqaba-elat: new evidence from liquefaction, seismic reflection, and paleoseismic data, *Tectonophysics,* **793,** 228596, doi: 10.1016/j.tecto.2020.228596.

Klinger, Y., Rivera, L. & Haessler, H., 1999. Active faulting in the Gulf of Aqaba: new knowledge from the Mw 7.3 earthquake of 22 November 1995, *Bull. seism. Soc. Am.,* **89**(4), 1025–1036.

Klinger, Y., Le Béon, M. & Al-Qaryouti, M., 2015. 5000 yr of paleoseismicity along the southern dead sea fault, *Geophys. J. Int.,* **202**(1), 313–327.

Le Béon, M. *et al.*, 2008. Slip rate and locking depth from GPS profiles across the southern Dead Sea Transform, *J. geophys. Res.,* **113**(B11) , doi:10.1029/2007JB005280.

Le Béon, M. *et al.*, 2010. Early holocene and late pleistocene slip rates of the southern dead sea fault determined from 10be cosmogenic dating of offset alluvial deposits, *J. geophys. Res.: Solid Earth,* **115**(B11), doi: 10.1029/2009JB007198.

Le Béon, M., Klinger, Y., Mériaux, A.-S., Al-Qaryouti, M., Finkel, R. C., Mayyas, O. & Tapponnier, P., 2012. Quaternary morphotectonic mapping of the wadi araba and implications for the tectonic activity of the southern dead sea fault, *Tectonics,* **31**(5), doi: 10.1029/2012TC003112.

Lefevre, M., Klinger, Y., Al-Qaryouti, M., Le Béon, M. & Moumani, K., 2018. Slip deficit and temporal clustering along the Dead Sea fault from paleoseismological investigations, *Sci. Rep.,* **8**(1) , doi:10.1038/s41598-018-22627-9.

Li, X., Jónsson, S. & Cao, Y., 2021. Interseismic deformation from sentinel-1 burst-overlap interferometry: application to the southern Dead Sea fault, *Geophys. Res. Lett.* , doi:10.1029/2021GL093481.

Lisowski, M., Savage, J. C. & Prescott, W. H., 1991. The velocity field along the san andreas fault in Central and Southern California, *J. geophys. Res.: Solid Earth,* **96**(B5), 8369–8389.

Liu, S., Shen, Z.-K., Bügmann, R. & Jónsson, S., 2020. Thin crème brûlée rheological structure for the Eastern California Shear Zone, *Geology* , doi:10.1130/G47729.1.

Lyberis, N., 1988. Tectonic evolution of the Gulf of Suez and the Gulf of Aqaba, *Tectonophysics,* **153**(1–4), 209–220.

Mahmoud, S., Reilinger, R., Mcclusky, S., Vernant, P. & Tealeb, A., 2005. GPS evidence for northward motion of the Sinai Block: implications for E. Mediterranean tectonics, *Earth planet. Sci. Lett.,* **238**(1–2), 217–224.

Mahmoud, Y. *et al.*, 2013. Kinematic study at the junction of the East Anatolian fault and the Dead Sea fault from GPS measurements, *J. Geodyn.,* **67,** 30–39.

Masson, F., Hamiel, Y., Agnon, A., Klinger, Y. & Deprez, A., 2015. Variable behavior of the Dead Sea Fault along the southern Arava segment from GPS measurements, *C. R. Geosci.,* **347**(4), 161–169.

McCaffrey, R., 2005. Block kinematics of the pacific-north america plate boundary in the southwestern united states from inversion of gps, seismological, and geologic data, *J. geophys. Res.: Solid Earth,* **110**(B7) , doi:10.1029/2004JB003307.

McCaffrey, R., 2009. Time-dependent inversion of three-component continuous gps for steady and transient sources in northern cascadia, *Geophys. Res. Lett.,* **36**(7) , doi:10.1029/2008GL036784.

McClusky, S., Reilinger, R., Mahmoud, S., Ben Sari, D. & Tealeb, A., 2003. GPS constraints on Africa (Nubia) and Arabia plate motions, *Geophys. J. Int.,* **155**(1), 126–138.

McKenzie, D., 1972. Active tectonics of the mediterranean region, *Geophys. J. Int.,* **30**(2), 109–185.

McKenzie, D., Davies, D. & Molnar, P., 1970. Plate tectonics of the red sea and east africa, *Nature,* **226**(5242), 243, doi: 10.1038/226243a0.

Meade, B. J. & Hager, B. H., 2005. Block models of crustal motion in southern california constrained by gps measurements, *J. geophys. Res.: Solid Earth,* **110**(B3) , doi:10.1029/2004JB003209.

Meghraoui, M., 2015. *Paleoseismic History of the Dead Sea Fault Zone,* eds Beer, M., Kougioumtzoglou, I., Patelli, E. & Au, I.K., Springer Berlin Heidelberg, Encyclopedia of Earthquake Engineering , doi:10.1007/978-3-642-36197-5_40-1.

Mohsen, A., Kind, R., Sobolev, S. V., Weber, M. & Group, D., 2006. Thickness of the lithosphere east of the dead sea transform, *Geophys. J. Int.,* **167**(2), 845–852.

Nuriel, P., Weinberger, R., Kylander-Clark, A., Hacker, B. & Craddock, J., 2017. The onset of the Dead Sea transform based on calcite age-strain analyses, *Geology,* **45**(7), 587–590.

Okada, Y., 1985. Surface deformation due to shear and tensile faults in a half-space, *Bull. seism. Soc. Am.,* **75**(4), 1135–1154.

Pe'eri, S., Wdowinski, S., Shtibelman, A., Bechor, N., Bock, Y., Nikolaidis, R. & van Domselaar, M., 2002. Current plate motion across the Dead Sea Fault from three years of continuous GPS monitoring, *Geophys. Res. Lett.,* **29**(14), 42–1-42-4.

Peltzer, G., Rosen, P., Rogez, F. & Hudnut, K., 1996. Postseismic rebound in fault step-overs caused by pore fluid flow, *Science,* **273**(5279), 1202–1204.

Piersanti, A., Nostro, C. & Riguzzi, F., 2001. Active displacement field in the suez-sinai area: the role of postseismic deformation, *Earth planet. Sci. Lett.,* **193**(1), 13–23.

Pietrantonio, G., Devoti, R., Mahmoud, S. & Riguzzi, F., 2016. Kinematics of the Suez-Sinai area from combined GPS velocity field, *J. Geodyn.,* **102,** 231–238.

Pinar, A. & Tükelli, N., 1997. Source inversion of the 1993 and 1995 Gulf of Aqaba earthquakes, *Tectonophysics,* **283**(1–4), 279–288.

Pollitz, F. F., 1997. Gravitational viscoelastic postseismic relaxation on a layered spherical earth, *J. geophys. Res.: Solid Earth,* **102**(B8), 17921–17941.

Quennell, A. M., 1958. The structural and geomorphic evolution of the dead sea rift, *Quart. J. Geol. Soc.,* **114**(1–4), 1–24.

Quennell, A. M., 1959. Tectonics of the dead sea rift, in *Proceedings of the 20th International Geological Congress,* Vol. **385,** pp. 403, Mexico.

Reilinger, R. *et al.*, 2006. Gps constraints on continental deformation in the africa-arabia-eurasia continental collision zone and implications for the dynamics of plate interactions, *J. geophys. Res.: Solid Earth,* **111**(B5) , doi:10.1029/2005JB004051.

Ribot, M., Klinger, Y., Jónsson, S., Avsar, U., Pons-Branchu, E., Matrau, R. & Mallon, F. L., 2021. Active faults' geometry in the gulf of aqaba, southern dead sea fault, illuminated by multibeam bathymetric data, *Tectonics,* **40**(4), doi.org/10.1029/2020TC006443.

Riguzzi, F., Pietrantonio, G., Piersanti, A. & Mahmoud, S. M., 2006. Current motion and short-term deformations in the suez-sinai area from gps observations, *J.Geodyn.,* **41**(5), 485–499.

Sadeh, M., Hamiel, Y., Ziv, A., Bock, Y., Fang, P. & Wdowinski, S., 2012. Crustal deformation along the dead sea transform and the carmel fault inferred from 12 years of gps measurements, *J. geophys. Res.: Solid Earth,* **117**(B8) , doi:10.1029/2012JB009241.

Savage, J., Lisowski, M. & Svarc, J., 1994. Postseismic deformation following the 1989 (m= 7.1) loma prieta, California, earthquake, *J. geophys. Res.: Solid Earth,* **99**(B7), 13757–13765.

Savage, J. C. & Burford, R. O., 1973. Geodetic determination of relative plate motion in central California, *J. geophys. Res.,* **78**(5), 832–845.

Scholz, C. H., 2002. *Earthquake Prediction and Hazard Analysis. In The Mechanics of Earthquakes and Faulting,* 2nd edn, pp. 351–414, Cambridge University Press , doi:10.1017/CBO9780511818516.009.

Shamir, G., Baer, G. & Hofstetter, A., 2003. Three-dimensional elastic earthquake modelling based on integrated seismological and InSAR data: the $M_w = 7.2$ Nuweiba earthquake, gulf of Elat/Aqaba 1995 November, *Geophys. J. Int.,* **154**(3), 731–744.

Smith-Konter, B. R., Sandwell, D. T. & Shearer, P., 2011. Locking depths estimated from geodesy and seismology along the san andreas fault system: Implications for seismic moment release, *J. geophys. Res.: Solid Earth,* **116**(B6) , doi:10.1029/2010JB008117.

Steinitz, G., Bartov, Y. & Hunziker, J., 1978. K-ar age determinations of some miocene–pliocene basalts in israel: their significance to the tectonics of the rift valley, *Geol. Mag.,* **115**(5), 329–340.

Tang, Z., Juliá, J., Zahran, H. & Mai, P. M., 2016. The lithospheric shear-wave velocity structure of saudi arabia: young volcanism in an old shield, *Tectonophysics,* **680,** 8–27.

Thomas, R., Parker, S. T. & Niemi, T. M., 2007. Structural damage from earthquakes in the second–ninth centuries at the archaeological site of aila in aqaba, jordan, *Bull. Am. Schools Orient. Res.,* **346**(1), 59–77.

Vergnolle, M., Pollitz, F. & Calais, E., 2003. Constraints on the viscosity of the continental crust and mantle from gps measurements and postseismic deformation models in western mongolia, *J. geophys. Res.: Solid Earth,* **108**(B10), doi: 10.1029/2002JB002374.

Wang, R., Lorenzo-Martín, F. & Roth, F., 2006. PSGRN/PSCMP—a new code for calculating co-and post-seismic deformation, geoid and gravity changes based on the viscoelastic-gravitational dislocation theory, *Comput. Geosci.,* **32**(4), 527–541.

Wdowinski, S., Bock, Y., Forrai, Y., Melzer, Y. & Baer, G., 2001. The GIL network of continuous GPS monitoring in Israel for geodetic and geophysical applications, *Israel J. Earth Sci.,* **50**(1), 39–48.

Wdowinski, S. *et al.*, 2004. Gps measurements of current crustal movements along the dead sea fault, *J. geophys. Res.: Solid Earth,* **109**(B5) , doi:10.1029/2003JB002640.

Weertman, J. & Weertman, J., 1964. *Elementary Dislocation Theory,* Macmillan Series in Materials Science, Macmillan.

Wessel, P., Smith, W. H., Scharroo, R., Luis, J. & Wobbe, F., 2013. Generic mapping tools: improved version released, *EOS, Trans. Am. geophys. Un.,* **94**(45), 409–410.

Wright, T., Parsons, B. & Fielding, E., 2001. Measurement of interseismic strain accumulation across the north anatolian fault by satellite radar interferometry, *Geophys. Res. Lett.,* **28**(10), 2117–2120.

Zilberman, E., Amit, R., Porat, N., Enzel, Y. & Avner, U., 2005. Surface ruptures induced by the devastating 1068 ad earthquake in the southern arava valley, dead sea rift, israel, *Tectonophysics,* **408**(1-4), 79–99.

SUPPORTING INFORMATION

Supplementary data are available at *GJI* online.

Figure S1: Observation epochs of the new GPS Network in the Gulf of Aqaba and 16 additional IGS stations used to impose the ITRF2014 reference frame. Red dots depict campaign site occupations. Blue and grey segments show the temporal coverage of continuous stations located in the Gulf of Aqaba and IGS stations, respectively.

Figure S2: Regional GPS velocity field in Sinai-fixed reference frame. Labelled stations correspond to the subset of the GIL network in Israel used to derive the Euler pole of the Sinai subplate relative to ITRF2014.

Figure S3: Effect of small fault strike variations ($\pm 5^\circ$) on model-predicted velocities across the Eilat fault (panel a) and Tiran-Arnona faults (panel b).

Figure S4: Same as Fig. 5 but considering all the GPS observations in the profiles (including outliers).

Figure S5: Same as panels (b)–(d) and (f) in Fig. 7 but assigning a dip of 65° to the Aragonese fault.

Figure S6: Comparison between residual velocities at seven near-fault GPS stations on the Arabian side of the gulf (TAYS, TAY1, MAG2, TB03, MAG1, RASH, GA29) assuming fully locked (panels a and b) and fully creeping scenarios (panels c and d) for the Arnona fault. Note the bias introduced in the latter case.

Table S1: Station information and observation epochs$^{(*)}$ of the new survey-mode GPS network established in the Gulf of Aqaba.

Table S2: Station coordinates, observed velocities in ITRF2014 and Sinai-fixed reference frame, 1σ uncertainties and adjustments. Campaign stations from the new GNSS network in the Gulf of Aqaba are indicated with an asterisk. Previously unpublished results from continuous stations operating near the gulf area are indicated with an (n) superscript. Permanent GNSS stations from the GIL network are marked with a (g) superscript.

Please note: Oxford University Press is not responsible for the content or functionality of any supporting materials supplied by the authors. Any queries (other than missing material) should be directed to the corresponding author for the paper.